

Manuscript

Press hardening of zinc-coated boron steels: role of steel composition in the development of phase structures within coating and interface regions

Henri Järvinen^{1*}, Mari Honkanen¹, Madan Patnamsetty¹, Sanna Järn², Esa Heinonen³, Hua Jiang⁴, and Pasi Peura¹

¹Laboratory of Materials Science, Tampere University of Technology, P.O. Box 589, FI-33101 Tampere, Finland

²SSAB Europe Oy, Harvialantie 420, FI-13300, Hämeenlinna, Finland

³Center of Microscopy and Nanotechnology, University of Oulu, P.O. Box 7150, FI-90014 Oulu, Finland

⁴Nanomicroscopy Center, Aalto University, P.O. Box 15100, FI-00076, Aalto, Finland

^{1*}) henri.jarvinen@tut.fi

Abstract

Zn and ZnFe coated 22MnB5 and 34MnB5 steels were subjected to the direct press hardening process in order to investigate the influence of steel composition on the resulting phase structures. Microstructures were characterized using advanced methods of microscopy. In addition, X-ray diffraction, glow discharge optical emission spectroscopy and thermodynamic calculations with Thermo-Calc® were carried out to support the analysis. The results indicate that the steel composition has a clear effect on the phase development within coating and interface regions. Whereas the behavior of the 22MnB5 was comparable to earlier investigations, a clearly non-conventional behavior of the 34MnB5 was observed: the formation of martensitic micro constituents, designated here as α' -Fe(Zn), were identified after die-quenching. The regions of the α' -Fe(Zn) formed mainly in vicinity of steel/coating interface and were emerged into the steel by sharing martensitic morphology with the base steel. The thermodynamic calculations suggest

that carbon is effective in stabilizing the γ -Fe(Zn) phase, which enables the formation of the α' -Fe(Zn) in fast cooling. Therefore, the higher initial C content of the 34MnB5 may result in the kinetic stabilization of the γ -Fe(Zn) as the inter-diffusion between Zn and Fe occurs during annealing. Simultaneously occurring carbon partitioning from α -Fe(Zn) to γ -Fe(Zn) could explain a clearly increased C content of the coating/steel interface as well as higher Zn contents in the α' -Fe(Zn) phase compared to 22MnB5. Actually, the present study shows that the same phenomenon occurs also in 22MnB5 steels, but in a much smaller scale. In Zn and ZnFe coated 34MnB5, the thickness of the α' -Fe(Zn) layer was increased with longer annealing times and at higher temperatures. The morphology of the α' -Fe(Zn) layer resembled plate-like martensite and can be assumed to be brittle. Regarding this, the formation of α' -Fe(Zn) interface layer needs to be taken into account in press hardening of 34MnB5 steels.

Keywords: Press hardening; Hot-dip galvanizing; Phase transformations; Electron backscatter diffraction; Focused ion beam; Transmission electron microscopy

1. Introduction

Hot-dip galvanized press hardening steels (PHS) have turned out to be appealing materials for car body components by providing unique combination of ultra-high strength and galvanic corrosion resistance [1]. Consequently, automotive manufacturers aim to increase the use of zinc-coated steels in the press-hardened components [2]. In general, continuous galvanizing is used to produce two types of zinc-based coatings for PHS: conventional zinc coating (Zn) and zinc-iron alloy coating (ZnFe), i.e., galvanized coating containing initially 8-12 % of iron. The ZnFe coating is obtained by using a lower Al content of the zinc bath, and by applying a post dip annealing treatment [3]. Both zinc-based coatings are applicable in press hardening technology, but ZnFe coating has higher thermal stability resulting in a broader processing window [4]. In addition, a suitability of electroplated ZnNi coatings have been investigated [5-7]. However, currently there are not any commercial solutions available utilizing the ZnNi coating [8].

The direct press hardening process combines three distinct steps: heating/austenitization of the blank, transferring from furnace to die, and a final step of hot forming and quenching performed in a water-cooled die. During these stages, zinc-based coatings undergo significant changes in their phase structure and composition. The coating reacts with the steel and becomes gradually more and more enriched with Fe through inter-diffusion, occurring between Zn from the coating and Fe from the steel [3,9]. The Fe-Zn phase diagram has been typically applied to understand the high temperature phase development of zinc-coated PHS. According to the diagram proposed by Burton and Perrot [10], the Fe-Zn system covers several phases as a function of Zn content when heated up to the typical annealing temperature of around 900 °C: pure zinc η , intermetallic Zn-Fe compounds ζ , δ , Γ_1 , and Γ_2 as well as solid solution α -Fe(Zn). The intermetallic Zn rich

phases melt during heating/annealing stage, but re-solidification of the coating occurs by the increasing Fe content and resulting formation of α -Fe(Zn). In the pure Fe-Zn system, the austenitic solid solution γ -Fe(Zn) phase may exist only above 900 °C.

PHS components are austenitized prior to hot forming, and thus high temperature phase development of hot-dip galvanized 22MnB5 has been extensively addressed in previous studies [4,11-15]. When conventionally heated up to the minimum austenitization temperatures of around 850 °C, the coating attains a structure consisting of a mixture of liquid and solid phases, i.e., Zn rich liquid phase and ferritic solid solution of Fe and Zn, i.e., α -Fe(Zn) [16,17]. The fraction of solid α -Fe(Zn) phase increases as a function of annealing time and temperature as the coating is enriched more and more with Fe, and some Zn is also oxidized in the surface to form ZnO [16]. The formation of ferritic α -Fe(Zn) is generally faster in ZnFe coating than in conventional Zn coating [4,13]. During the subsequent die-quenching step, liquid (if still present) and some of the α -Fe(Zn) phase transforms to the Zn rich Γ -Fe₃Zn₁₀ phase (hereafter referred to as Γ -ZnFe), and the remaining α -Fe(Zn) is stabilized when the material is quickly cooled into room temperature [18]. Thus, a short annealing tends to result in the layered phase structure: ZnO (oxide) on the top, some intermetallic Γ -ZnFe phase in the middle, and solid solution of α -Fe(Zn) on the bottom. Regardless of the oxide layer, a coating consisting only of a solid α -Fe(Zn) phase can be attained with prolonged soaking times [12,19,20]. At typical annealing temperatures of 900 °C, the maximum Zn content of α -Fe(Zn) is around 35 %, which is retained when the steel is quenched [18]. It has been observed that the Zn content of the α -Fe(Zn) phase decreases only slightly towards the coating/steel interface [9]. More interestingly, there is a sharp drop of the Zn content after reaching the α -Fe(Zn)/steel interface [9].

According to earlier studies [9,12,19-21] the final Zn content and galvanic capacity of the press-hardened coating is determined by the coating type, initial coating thickness and annealing parameters. When it comes to the influence of annealing parameters, a constant decrease in the Zn content of the coating occurs as a function of annealing time [9,19]. It has been also widely noted [9,12,19-22] that the coating thickness increases significantly during the thermal cycle of the direct press hardening process. Janik et al. [9] pointed out that the coating growth occurs by means of inter-diffusion as the grain boundaries of the α -Fe(Zn) phase move towards steel. Regarding this, the coating layer gets thicker at the expense of steel. The contribution of steel alloying elements has not been paid much attention, but is obviously worth considering due to nature of the inter-diffusion layer. Accordingly, Janik et al. [22] used a FactSage software to calculate a phase diagram for 22MnB5-Zn system instead of the conventionally used Fe-Zn. It was noticed that the phase region of austenitic γ -Fe(Zn) phase is significantly larger compared to the pure Fe-Zn system. Therefore, the γ -Fe(Zn) phase may be theoretically present at typical austenitization temperatures around 900 °C [22]. If this is the case, the austenitic phase constituents of the coating might transform into martensite during subsequent quenching. However, none of the previous studies has addressed the formation of martensitic micro constituents α' -Fe(Zn) in Zn or ZnFe coated 22MnB5.

Currently, there is a demand for novel PHS providing tensile strength reaching 2000 MPa [8]. In order to attain the desired strength, steels of 34MnB5 type with the C content around 0.35 %, have been recently investigated [23-25]. None of the previous studies has addressed the high temperature phase development of zinc-coated 34MnB5 steels at least known to the authors. Based on the previous study of Janik et al. [22], the steel composition may have a significant effect on the high temperature phase equilibrium of the Fe-Zn system. In the present study, Zn

and ZnFe coated boron steels are subjected to the direct press hardening process and phase structures of the die-quenched samples are comprehensively analyzed and compared. The results will show significant differences between 22MnB5 and 34MnB5 grades. Finally, the behavior of both grades and the role of steel composition will be discussed in detail.

2. Materials and methods

2.1 Test materials

The as-received materials consisted of two commercial 22MnB5 steels along with two commercial 34MnB5 steels, both coated with Zn and ZnFe coatings. The details and chemical compositions of the as-received steels are described in Table 1. The expressed A_{c3} temperatures were calculated using the equation presented by Kasatkin et al. [26].

Table 1. Details and chemical compositions (wt-%) of the as-received test materials.

Steel	Sheet thickness	Coating weight (side/side)	C %	Si %	Mn %	Cr %	Al %	B %	A_{c3} (°C)
22MnB5-Zn	1.5 mm	50/50 g/m ²	0.24	0.26	1.18	0.20	0.033	0.0029	831
22MnB5-ZnFe	1.5 mm	70/70 g/m ²	0.23	0.26	1.24	0.21	0.029	0.0031	830
34MnB5-Zn	1.1 mm	50/50 g/m ²	0.35	0.26	1.30	0.15	0.033	0.0026	800
34MnB5-ZnFe	1.5 mm	70/70 g/m ²	0.35	0.25	1.32	0.15	0.033	0.0014	803

As indicated in Table 1, the differences in the chemical compositions are small except to the difference in C contents between the 22MnB5 and 34MnB5 grades. The received samples of the 34MnB5-Zn had a smaller sheet thickness compared to the samples of other investigated steels.

2.2 Press hardening experiments

Press hardening experiments were carried out using an experimental press hardening equipment described more in detail in an earlier study [27]. The experiments were conducted for steel sheet samples of the size of 110 x 100 x (sheet thickness). The annealing parameters, described specifically in Table 2, were chosen to examine a wide range of annealing cycles. The cycles were determined based on two methods. Firstly, samples of all steels were subjected to short (180 s) and long (450 s) annealing times at typical austenitization/target temperature of 900 °C. Secondly, additional samples of 34MnB5-Zn were also annealed based on the time required for reaching the austenite transformation temperature A_{c3} at the predefined target temperatures of 880 °C and 930 °C. These temperatures were chosen in order to examine a wider range of austenitization temperatures applicable for zinc-coated PHS. With this method, short ($A_{c3}+30$ s) and long ($A_{c3}+330$ s) annealing cycles were investigated. After the annealing, a sample was transferred to the die within 3 s and subsequently quenched between two water-cooled steel blocks in the size of 120 x 100 x 30 mm. The pressure was maintained for 30 s allowing the samples to cool down below 100 °C, which is clearly below the M_f temperature of both 22MnB5 and 34MnB5 steels. An adequate cooling rate of samples (at least 80 °C/s) was ensured and predominantly martensitic microstructure of steel was obtained in cases where fully austenitization of steel was attained. The sample temperature was measured using K-type thermocouples spot welded onto the samples.

Table 2. Parameters of the examined annealing cycles. The attained peak temperature of each cycle is expressed in the parenthesis.

Steel	880 °C: A _{c3} +30 s, A _{c3} +330 s	900 °C: total dwell times	930 °C: A _{c3} +330 s
22MnB5-Zn		180 s (820 °C), 450 s (900 °C)	
22MnB5-ZnFe		180 s (890 °C), 450 s (900 °C)	
34MnB5-Zn	170 s (850 °C), 470 s (880 °C)	180 s (890 °C), 450 s (900 °C)	430 s (930 °C)
34MnB5-ZnFe		180 s (890 °C), 450 s (900 °C)	

The peak temperature values expressed in Table 2 imply that the differences in the coating characteristics caused fluctuation in the heating rates between ZnFe and Zn coated samples. It is known that the matte surface of the ZnFe coated sheets promotes faster heating. The heating rate affects the resulting phase structure, especially in the case of short annealing cycles, in which the attained peak temperature did not necessarily reach the target temperature. In addition, the smaller sheet thickness of the 34MnB5-Zn samples (1.1 mm) accelerated the heating compared to the 22MnB5-Zn samples (1.5 mm).

2.3 Microstructural characterization

Press hardened samples were sectioned for the microstructural analysis carried out with an optical microscope and scanning electron microscopes (SEM). The samples were ground using abrasive SiC papers, polished with 3 and 1 µm diamond suspensions. A need of etching procedure was determined by the type of analysis to be carried out. The samples observed with an optical microscope Nikon Eclipse MA 100 were etched for 5 s using 2 % Nital solution. The cross-sections were also analyzed by using a Zeiss Ultra Plus field emission gun scanning electron microscope (FEG-SEM) equipped with energy dispersive X-ray spectrometer (EDS) INCAx-act

silicon-drift detector, Oxford Instruments. Backscattered electron (BSE) imaging with the acceleration voltage of 5 kV was utilized to identify different phase regions with compositional differences from unetched samples. Elemental point analysis and mapping by EDS with the acceleration voltage of 15 kV were carried out for both unetched and etched samples to support the visual phase identification. The FEG-SEM was also fitted with an HKL Premium-F Channel EBSD (Electron Backscatter Diffraction) system with a Nordlys F400 detector that was used in crystallographic analysis. The samples used in the EBSD measurements were final polished using colloidal silica suspension (0.04 μm). Step size of 0.1 μm and acceleration voltage of 20 kV were used and Channel 5 data analysis package was used to construct EBSD maps. In addition, a Philips XL30 SEM equipped with Anton Paar μ -Indenter 5 (Vickers) was employed to evaluate micro mechanical properties of the phase constituents. The weight of 5 g and the dwell time of 15 s was used in indentation.

A high-resolution (scanning) transmission electron microscope (HR-TEM (S)) JEOL 2200FS operated at 200 kV was used for analyzing phase constituents of the die-quenched samples with higher spatial accuracy. The microscope is equipped with two aberration correctors (CEOS GmbH) for high-resolution imaging and an EDS detector (Jeol Si(Li)) for elemental analysis. Elemental line scans and point analysis by EDS in STEM mode were carried out to analyze chemical compositions of the phases with high spatial resolution. Acceleration voltage of 200 kV was used in (S)TEM analysis. Site-specific TEM samples were manufactured by using a FEI Helios Nanolab 600 DualBeam system using standard focused ion beam (FIB) TEM preparation techniques.

2.4. X-ray diffraction (XRD)

XRD analysis with Cu K α -radiation (20° - 75°, step size 0.0260°, 40 kV, 45 mA) using a Panalytical Empyrean X-ray diffractometer were carried out in the selected cases to support the phase structure analysis of the press hardened coatings. The measurements were carried out on the surface plane of the samples with the 2 θ scan axis and incident angle of 15°.

2.5. Elemental analysis with glow discharge optical emission spectroscopy (GDOES)

A GDA750 glow discharge optical emission spectroscope (Spectrums Analytik GmbH) was used to measure elemental depth profiles of the selected samples in a die-quenched state. The measurements were performed in DC mode with a voltage of 700 V at a constant current of 20 mA. The sputtering time was determined so that the measuring depth of approximately 40 μ m was attained. The sputtering area was 4 mm in diameter and duplicate measurements per sample were carried out.

2.6. Thermodynamic calculations

A thermodynamic calculation software Thermo-Calc® was utilized to analyze the effect of C content on the Fe-Zn phase equilibrium. First, a ternary Fe-Zn-C system were calculated using the TCFe9 database. Then, isoplethal sections with different C contents were reviewed and selected. In addition, a graph presenting the maximum solubility of Zn in austenite at typical annealing/austenitization temperature of 900 °C as a function of C content was plotted. Fig. 1 presents the outcomes of the thermodynamic calculations.

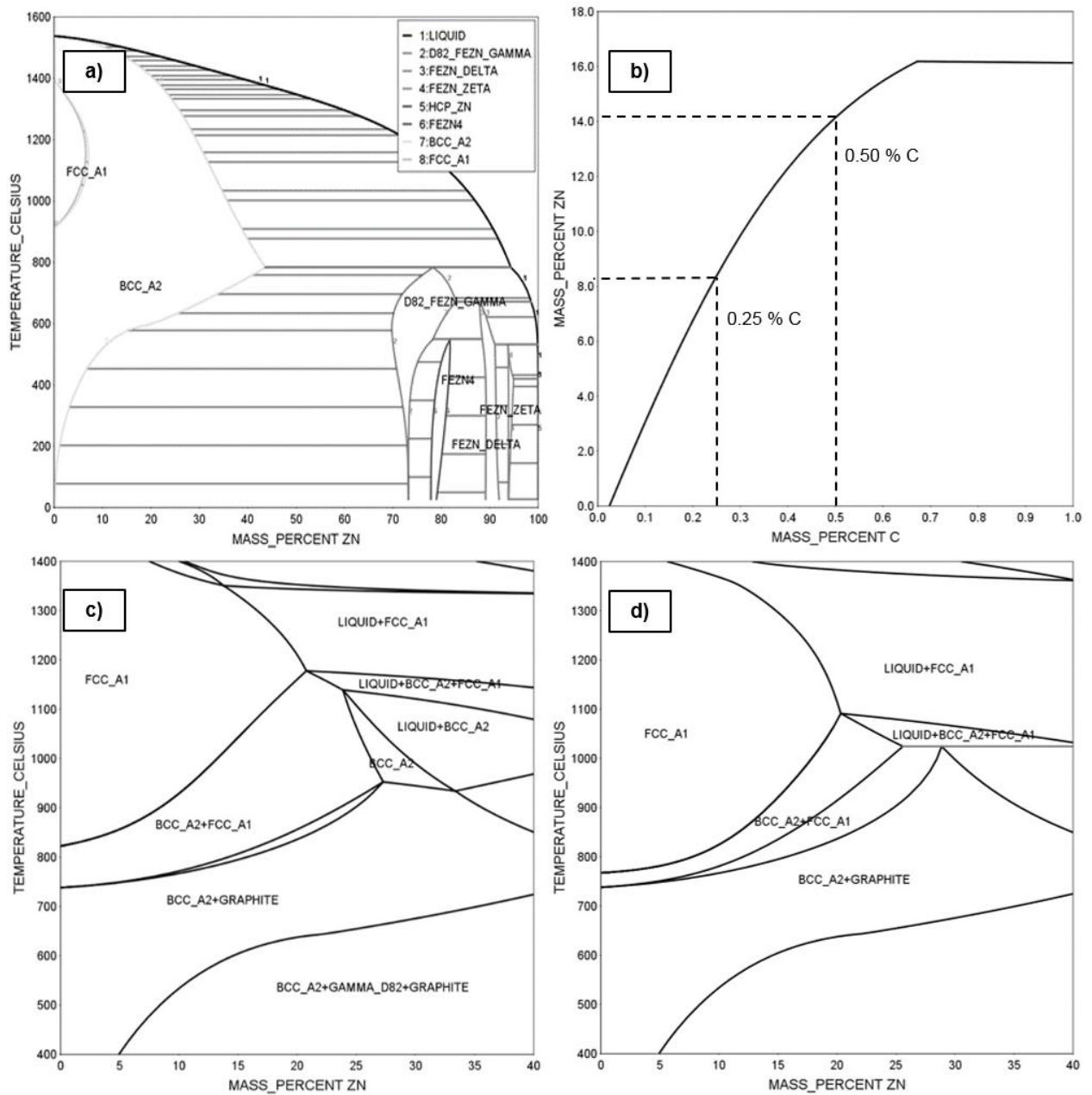


Fig. 1. a) Calculated Fe-Zn phase diagram. b) Maximum solubility of Zn in austenite (FCC_A1) at 900 °C as a function of C content. Isoplethal sections of the Fe-Zn-C system with C contents of; c) 0.25 wt-%; d) 0.50 wt-%. Designation BCC_A2 refers to the ferritic solid solution α -Fe(Zn).

The calculated Zn-Fe system (Fig. 1a) shows that the stability area of austenitic FCC_A1 phase, i.e., γ -Fe(Zn) is very limited. Accordingly, austenitic γ -Fe(Zn) is not present at typical

austenitization temperature of 900 °C. Overall, the calculated diagram is almost identical to the diagram presented by Burton and Perrot [10]. The maximum solubility of Zn in γ -Fe(Zn) is 6 % and is attained at around 1100 °C. As can be seen in Fig. 1b, the incorporation of C has a significant effect on the solubility of Zn in austenite. At 900 °C, the solubility is increased as a function of C content up to 0.67 wt-% after which the solubility of Zn levels off. The presented isoplethal sections of the Fe-Zn-C system (Figs. 1c and 1d) imply that the increasing C content extends the stability area of austenitic FCC_A1 phase, i.e., γ -Fe(Zn) moves towards lower temperatures and higher Zn contents. With the C content of 0.25 wt-%, the maximum amount of Zn in γ -Fe(Zn) at 900 °C is around 8 wt-%. When the C content is doubled up to 0.50 wt-% the solubility of Zn is increased to around 14 wt-%. It can be also noticed that the C content of 0.25 wt-% extends the stability area of the two-phase region BCC_A2 + FCC_A1, i.e., consisting of α -Fe(Zn) + γ -Fe(Zn) phases. However, this region is contracted with the increase in C content at the expense of austenitic phase. This suggests that when the C content of the system is increased from 0.25 wt-% to 0.50 wt-%, a larger amount of α -Fe(Zn) is transformed into γ -Fe(Zn).

3. Results

3.1. Phase structures

Fig. 2 presents optical and SEM (BSE) micrographs of the die-quenched 22MnB5-Zn (Figs. 2a-d) and 22MnB5-ZnFe (Figs. 2e-h) samples annealed for 180 and 450 s at 900 °C.

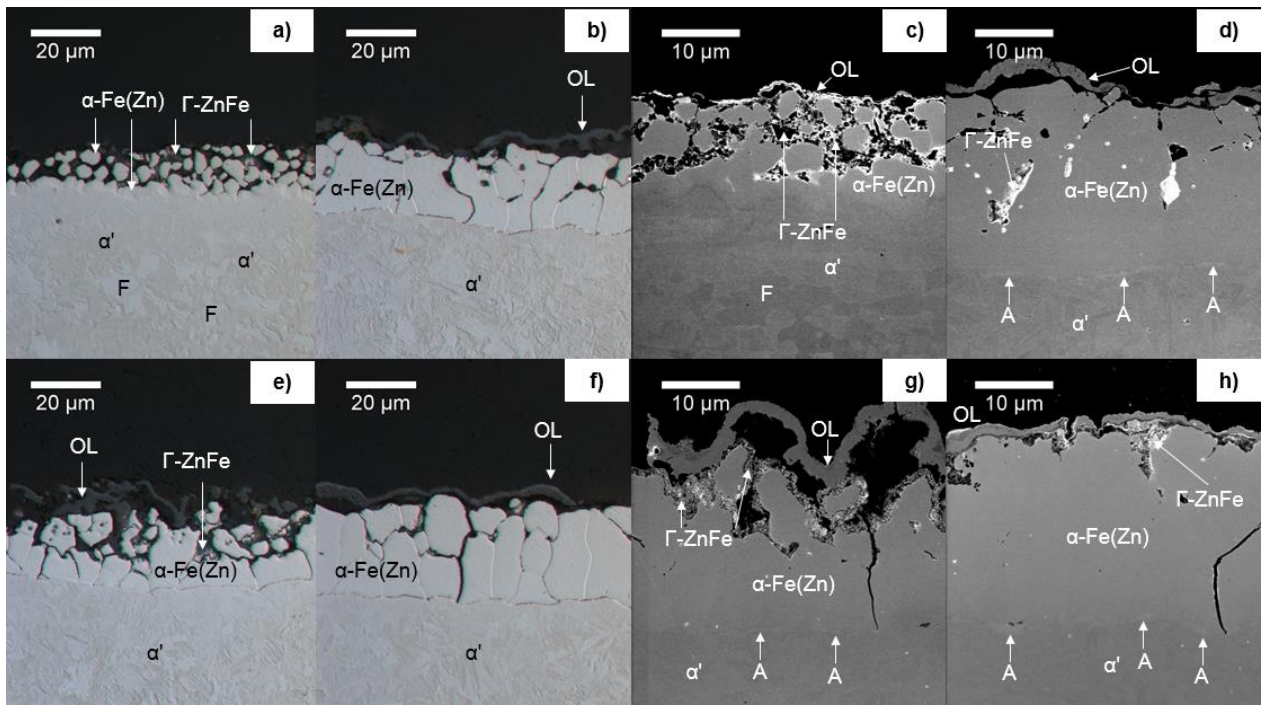


Fig. 2. Optical micrographs of the die-quenched 22MnB5-Zn annealed for; a) 180 s; b) 450 s at 900 °C along with SEM (BSE) micrographs corresponding to; c) 180 s; d) 450 s. Optical micrographs of the die-quenched 22MnB5-ZnFe annealed for; e) 180 s; f) 450 s at 900 °C along with SEM (BSE) micrographs; g) 180 s; h) 450 s.

Fig. 2a indicates that except for the oxide layer (OL), the die-quenched coating of 22MnB5-Zn (180 s/900 °C) consists of two phases. The EDS point analysis confirmed that the dark regions of the etched sample (Fig. 2a) correspond to the intermetallic Γ -ZnFe phase, which should be ideally seen as bright in the BSE image (Fig. 2c) due to high Zn content. To clarify, the Γ -ZnFe phase can be easily dissolved or partially pulled out during conventional metallographic sample preparation, despite ignoring the metallographic etching. Thus, also the dark areas below the oxide layer are Γ -ZnFe. However, those regions emit less electron signal due to lower topographical position. The other major phase, α -Fe(Zn), appears as light grey in the BSE image (Fig. 2c). The ferritic α -Fe(Zn) has dissolved significantly less compared to the Γ -ZnFe due to

smaller Zn content. As expressed in Table 2, the sample annealed for 180 s reached only a temperature of about 820 °C. This has resulted in incomplete austenitization of the steel; the presence of ferrite islands F among martensite α' supports this observation. A comparison between the structures shown in Figs. 2a and 2b imply that the structure of 22MnB5-Zn has changed significantly as a function of annealing time. The longer annealing time of 450 s has led to notable increase in the amount of the α -Fe(Zn) at the expense of the Γ -ZnFe. In addition, a clear increase in the coating thickness can be observed. More interestingly, the BSE image (Fig. 2d) reveals small bright regions designated as A in vicinity of the steel/coating interface. The obtained contrast between the regions of A, α -Fe(Zn), and martensitic base steel α' indicates that also the regions of A contain Zn. It is, however, difficult to verify if the contrast is actually obtained from distinct micro constituents or simply from the steel/coating interface.

Based on the phase structures shown in Figs. 2e and 2f, the behavior of ZnFe coated 22MnB5 is comparable to the Zn coated 22MnB5 samples in a general level: the amount of α -Fe(Zn) is markedly increased as a function of annealing time. However, due to faster heating rate along with the initial Fe content of the ZnFe coated sheets, larger amount of α -Fe(Zn) phase has been formed in the 22MnB5-ZnFe after a short annealing time of 180 s (Fig. 2e). The bright regions seen in the BSE-image (Fig. 2g) imply that small amounts of Γ -ZnFe phase were present in the upper parts of the coating - even after the longer annealing time of 450 s (Fig. 2h). These BSE images reveal thin brighter regions designated as A near the steel/coating interface (Figs. 2e and 2h). This observation is similar to the 22MnB5-Zn samples as discussed above (Fig. 2d). The thickness of these regions exceeds only a thickness of around 0.5 μm , and thus they are not clearly identifiable in the optical micrographs that were captured by observing etched cross-sections.

Fig. 3 presents optical and SEM (BSE) micrographs of the die-quenched 34MnB5-Zn (Figs. 3a-d) and 34MnB5-ZnFe samples (Figs. 3e-h) annealed for 180 and 450 s at 900 °C.

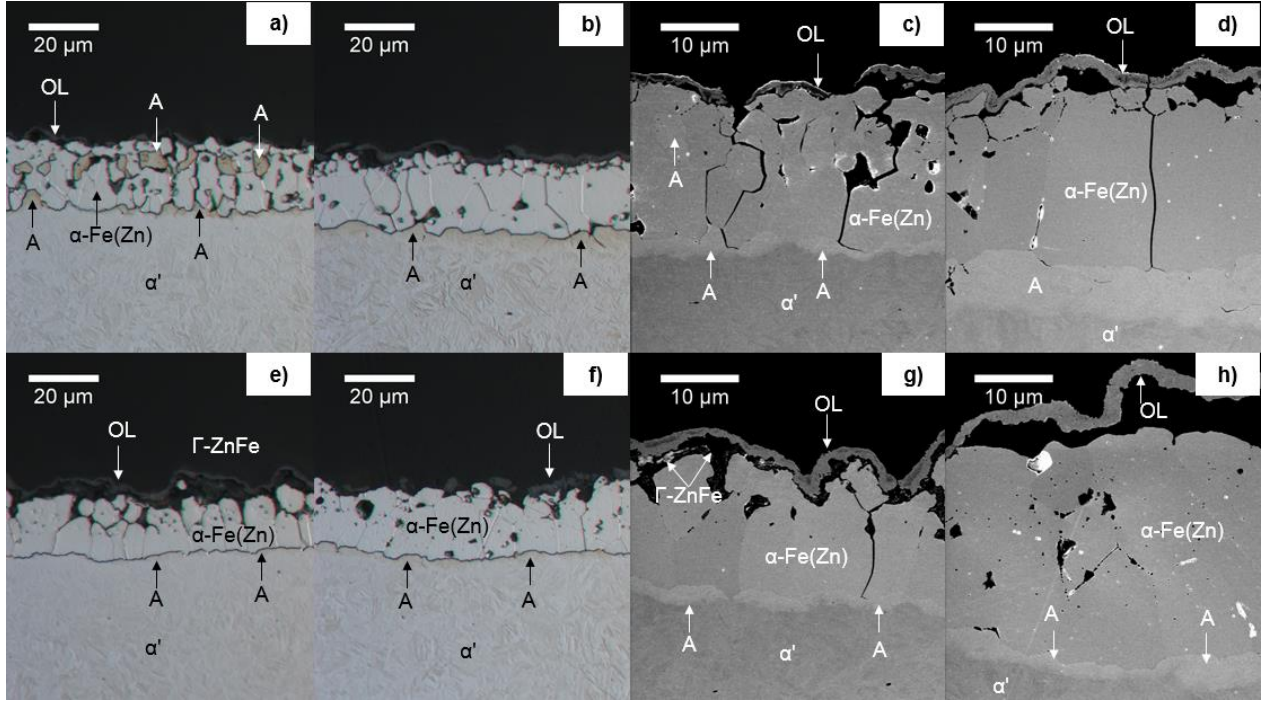


Fig. 3. Optical micrographs of the die-quenched 34MnB5-Zn annealed for; a) 180 s; b) 450 s at 900 °C along with SEM (BSE) micrographs corresponding to; c) 180 s; d) 450 s. Optical micrographs of the die-quenched 34MnB5-ZnFe annealed for; e) 180 s; f) 450 s at 900 °C along with SEM (BSE) micrographs; g) 180 s; h) 450 s.

Fig. 3a shows that the press hardened coating of 34MnB5-Zn contains two distinct phases after a short 180 s soak. However, the coating do not seem to contain any regions of the zinc rich Γ -ZnFe phase. 34MnB5-Zn had a smaller sheet thickness of 1.1 mm, which accelerated the heating of the sheet, in particular compared to 1.5 mm thick Zn coated sheets. Consequently, the sheet temperature reached 890 °C even in case of the shorter annealing cycle. Regarding this, higher amount of α -Fe(Zn) can be observed in 34MnB5-Zn by comparing the structures presented in

Figs. 3a and 2a. Here, the higher peak temperature of 34MnB5-Zn has resulted in the complete austenitization of the steel, and thus fully martensitic microstructure has been attained after fast cooling. In the case of 34MnB5-Zn (Fig. 3a), several regions designated as A are present in vicinity of the steel/coating interface. In addition, islands with the same appearance exist also in the upper parts of the coating and have been thus correspondingly marked using letter A. It is clear that the regions of A have not dissolved in a similar way as Zn rich Γ -ZnFe during the metallographic etching. As indicated in Fig. 3a, the etching depth is also different from α -Fe(Zn). In turn, the BSE image (Fig. 3c) of the unetched sample do not reveal strong contrast between the islands of A and α -Fe(Zn). This suggests that the micro constituents of A must also have relatively high Zn content. After the prolonged annealing time of 450 s, the regions of A are only present near the steel/coating interface. Actually, these regions appear in the form of a continuous layer (Fig. 3b). The thickness of this layer has been clearly increased with the prolonged soak. Surprisingly, no clear increase in the thickness of the α -Fe(Zn) layer can be observed between the 180 s and 450 s annealed samples (Fig. 3a and 3b). Instead, another notable observation can be made regarding the position of the steel/coating interface. As indicated in the BSE images (Figs. 3c and 3d), the steel/coating interface, i.e., the threshold between dark and light grey areas, has clearly settled in the lower position than in the optical micrographs; there the interface is formed between α -Fe(Zn) and A.

The optical micrograph (Fig. 3e) of the 34MnB5-ZnFe annealed for 180 s do not reveal any regions of A in the upper parts of the coating as observed in the case of 34MnB5-Zn (Fig. 3a). Instead, some Γ -ZnFe is still present in the 180 s annealed sample (Fig. 3g). However, similar to the 34MnB5-Zn, the ZnFe coated 34MnB5 samples show a layer of A near the steel/coating interface (Figs. 3f and 3e). This layer is much better distinguishable in the BSE images presented

in Figs. 3g and 3h. Similar to the 34MnB5-Zn, the thickness of the A is somewhat larger in the samples that were annealed for 450 s (Fig. 3d). It can be concluded that the formation of the micro constituents of A has clearly occurred in both 34MnB5 grades, but has been the most multidimensional in the case of 34MnB5-Zn samples.

Fig. 4 presents the XRD results for the 34MnB5-Zn annealed for 180 and 450 s at 900 °C.

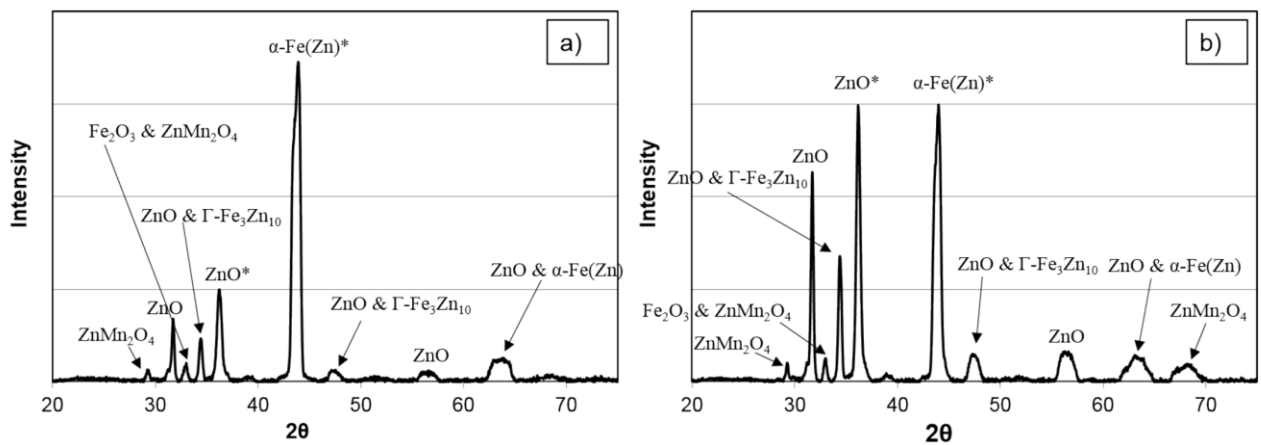


Fig. 4. Results of the X-ray diffraction measurements for; a) 34MnB5-Zn annealed for 180 s; b) 450 s. The main intensity peaks of ZnO and α -Fe(Zn) are marked with asterisk.

As can be seen in Fig. 4 the same phases were identified in both cases. There do not exist individual peaks for the islands of A (Fig. 3a). The intensities of the Γ -Fe₃Zn₁₀ phase, i.e., Γ -ZnFe are very low in both cases. Actually, the main intensity peak of the Γ -Fe₃Zn₁₀ that should appear at around 42.5°, were not observed. However, the Γ -Fe₃Zn₁₀ peaks of smaller intensities were found as superimposed with ZnO peaks indicating that the amount of Γ -ZnFe is very small. Hence, the XRD results are in line with the phase structures shown in Fig. 3. However, the amount of ZnO is clearly higher after the longer annealing time of 450 s, which is also supported by the microscopy analysis (Fig. 3).

Micro indentation was combined with SEM imaging in order to evaluate micro-mechanical properties of the formed phase constituents. A die-quenched 34MnB5-Zn sample annealed for 430 s at 930 °C was selected for the hardness measurements. The analysed sample was etched for 1 s using Nital 2 %. Fig. 4 shows an SEM image together with the Vickers hardness indentation marks.

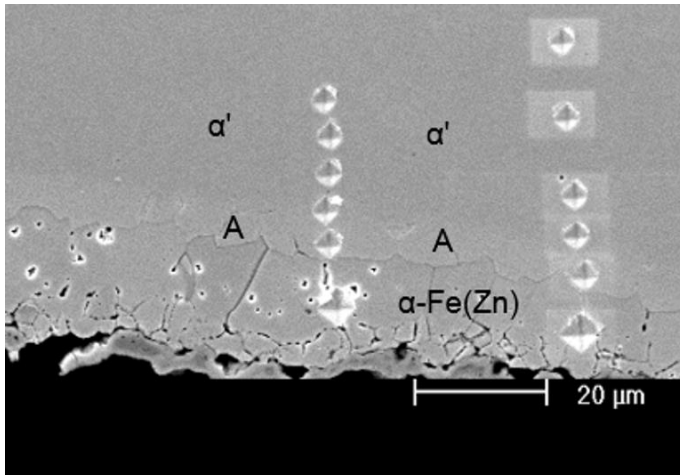


Fig. 5. SEM image showing Vickers indentation marks (HV 0.5 g) in identified layers of a 34MnB5-Zn sample annealed for 430 s at 930 °C.

The results of micro indentation (Fig. 5) indicate that ferritic α -Fe(Zn) phase is softer compared to the regions of A and martensitic base steel α' . The hardness values measured from the regions of A showed slightly lower values than the martensite of the base steel α' . This result suggests that micro constituents of A are also martensitic.

3.2. Chemical compositions

In order to emphasize the observed phenomenon regarding the formation of the aforementioned micro constituents of A, additional samples of 34MnB5-Zn were subjected to a wider range of

austenitization parameters prior to die quenching (Table 2). Accordingly, selected samples were analyzed with SEM-EDS. Fig. 6 presents BSE-images of the unetched samples, secondary electron (SE) images of the etched samples together with superimposed EDS point analysis results (Zn wt-%), and EDS maps (ZnK α) of the corresponding areas.

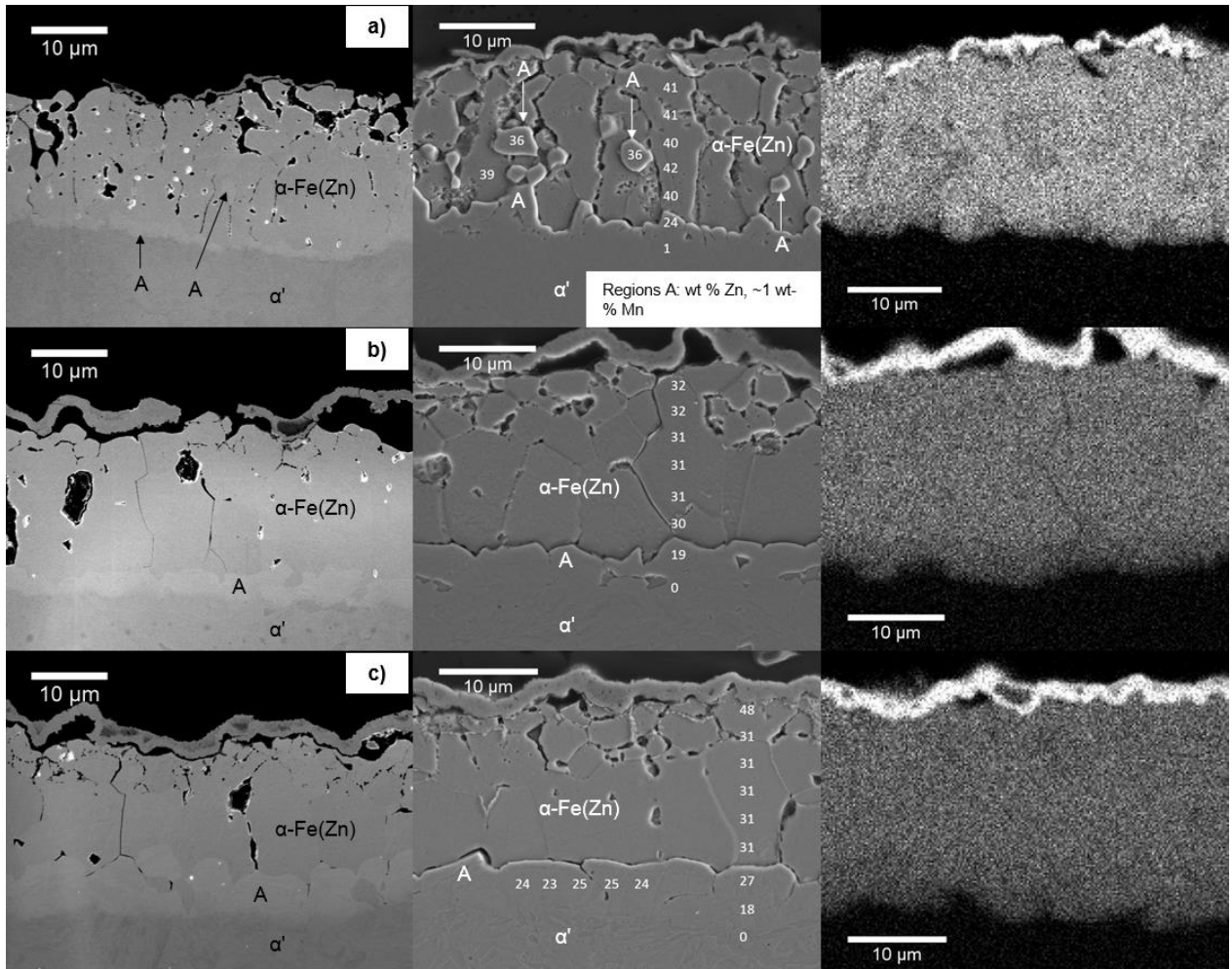


Fig. 6. BSE-images (left column), SE-images together with superimposed EDS point analysis results (Zn wt-%) (middle column), and EDS maps (ZnK α) (right column) for 34MnB5-Zn annealed for; a) 170 s at 880 °C; b) 470 s at 880 °C; c) 430 s at 930 °C.

According to the EDS point analysis, the islands of A contain surprisingly high amount of Zn, but slightly less than the surrounding α -Fe(Zn) phase (Fig. 6a, left). Considering the typical interaction volume of SEM-EDS, it is possible that ZnK α signal has been gathered from α -Fe(Zn) possibly existing behind the islands of A. Both EDS point analysis (Fig. 6a, middle) and mapping (Fig. 6a, right) indicate that the corresponding regions give only a little less ZnK α signal than the regions of α -Fe(Zn). As can be seen in the SE image of the etched sample (Fig. 6a, middle), the regions of A are in a higher position compared to the α -Fe(Zn) phase. Since there is only a small difference in the measured Zn contents, it can be thought that the amount of some other elements is markedly different compared to the α -Fe(Zn). However, the only difference observed with the EDS was the Mn content: the islands of A gave values of around 1 wt % Mn, whereas the amount of Mn was clearly lower in α -Fe(Zn).

A comparison of the BSE images (Fig. 6, left column) shows a pronounced formation of A as a function of annealing temperature and time: the layer of A is as thickest for the sample that was annealed for 430 s at 930 °C (Fig. 6c, left). In this respect, the formation of A is connected to the annealing parameters and is progressed due to propagation of the high temperature diffusion. According to presented EDS maps, it is evident that the layer A formed in the vicinity of the steel/coating interface contains a significant amount of Zn, e.g., between 23 and 25 wt-% as indicated in the SE image (Fig. 6c, middle). It can be also confirmed the interface seen in the SE-images (etched samples) is vertically in a lower position than in the Zn-EDS maps (Fig. 6, left column).

Elemental GDOES depth profiles for the selected die-quenched samples are presented in Fig. 7.

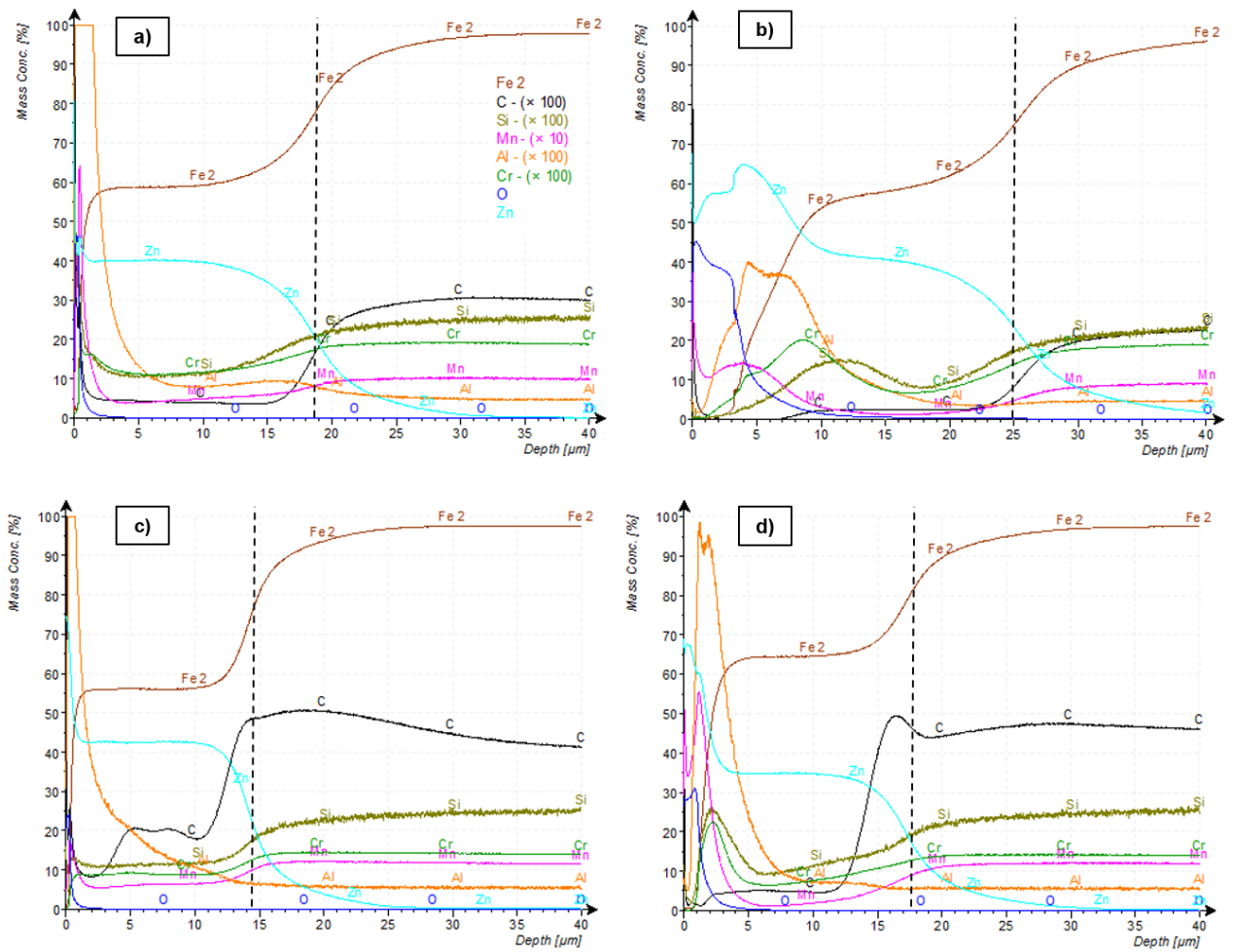


Fig. 7. Elemental GDOES profiles for; a) 22MnB5-Zn (450 s/900 °C); b) 22MnB5-ZnFe (450 s/900 °C); c) 34MnB5-Zn (170 s/880 °C); d) 34MnB5-Zn (430 s/930 °C). The curves of other alloying elements are omitted for clarity. The steel/coating interface, originally defined according to the derivative curve of the Fe content, is marked with a dashed vertical line. The legend presented in a) is the same for all graphs. (For interpretation of the references to colour in this figure legend, the reader is referred to the web version of this article).

The measured GDOES profiles (Fig. 7) show the amount of elements as a function of distance from the surface. The graphs indicate that the C contents, measured from the depths corresponding to the regions of the steel/coating interface, are different from the values that were obtained from the chemical analysis of the steels (Table 1). In the case of 22MnB5 samples (Figs.

7a and 7b), the measured C content beneath the steel/coating interface is only 0.10-0.15 wt-%. However, in the analysed 22MnB5-Zn sample (Fig. 7a), the values are 0.30 wt-% only some micrometers deeper, which exceeds the chemical composition of the steel. It needs to be noted that the measured values are largely averaged due to a relatively large region analyzed with a 4 mm sputtering diameter. As a consequence, the wavy interface of the corresponding die-quenched sample (Fig. 2f) inevitably results in the averaging of the C contents between the regions of ferritic α -Fe(Zn) and martensite of the base steel within the depth of approximately 5 μ m. Considering the nature of the GDOES method, the average C content can be evaluated to be around 0.25 wt-% near the steel/coating interface, since the small amount of C signal from the α -Fe(Zn) phase decreases the values around the determined interface marked with a dashed line. In the case of 34MnB5-Zn samples, the measured C content reaches significantly higher values compared to the steel compositions, i.e., about 0.50 wt-% near steel/coating interface (Figs. 7c and 7d). This result suggests that the layer designated as A in the previous Figs. 2-4, contains significant amount of C. Furthermore, it is evident that the region of the steel/coating interface is enriched with C. The enrichment can be seen in particular in the curves of the 34MnB5 samples. Regarding this, the measured difference in C contents between the investigated 22MnB5 and 34MnB5 steels is clearly larger, i.e., approximately 0.25 wt-% on average, than the difference in chemical compositions being about 0.12 wt-%.

As shown earlier in Fig. 6c (left), the upper layer of the coating in the 34MnB5 (430 s/930 °C) sample consists only of the α -Fe(Zn) phase. Accordingly, the GDOES profile (Fig. 7d) suggests that the C content of the α -Fe(Zn) phase is low, around 0.05 %. The result is reasonable since the solubility of C in ferrite is known to be very limited. In turn, the 34MnB5-Zn (170 s at 880 °C) contained the islands of A, and for the most part, α -Fe(Zn) phase (Fig. 6a). In this case, the

corresponding GDOES profile (Fig. 7c) reveals that especially the C content is at higher level, i.e., around 0.20 wt-%. The comparison of Figs. 7c and 7d suggests that also the Mn content is higher in the sample annealed for 170 s at 880 °C. The previously presented EDS analysis (Fig. 6a, middle), support this results. Therefore, it seems evident that the islands of A present in the upper parts of the coating, contain significantly higher amount of C, and probably also Mn, than the ferritic α -Fe(Zn) phase. The comparison of the chemical composition of steels (Table 1) and GDOES profiles (Fig. 7) suggests that the measured Mn contents in the vicinity of the steel/coating interface are slightly higher in 34MnB5 grades. For 34MnB5, the measured Mn content is around 0.9-1.0 wt-% near the interface, whereas for 22MnB5 the amount is approximately 0.7-0.8 wt-%. This result suggests that Mn does not certainly enrich towards steel/coating interface. However, the GDOES profiles imply that Mn tends to enrich in the oxide layer, which can be clearly seen in particular in Figs. 7a and 7d. The curves of Cr and Si do not show significant differences between 22MnB5 and 34MnB5 or either similar type of enrichment as C. The curves of Zn, Cr and Si show more fluctuation in 22MnB5-ZnFe sample (Fig. 7b), but this is believed to be caused by the presence of small amount of Γ -ZnFe phase in the coatings.

Fig. 7 shows that the curve profile of Al is somewhat different in 22MnB5-ZnFe (Fig. 7b) compared to the others. In general, Al tends to migrate towards surface to oxidize as reported for example by Autengruber et al. [16]. This behavior can be clearly seen in the curves of the 34MnB5-Zn samples (Figs. 7a, 7c, and 7d). In 22MnB5-ZnFe (Fig. 7b), the measured Al profile is different due to two reasons. Firstly, the initial Al content is naturally lower in ZnFe coatings due to lower Al content of the zinc bath. Secondly, the thickness of the oxide layer in the longer annealed 22MnB5-ZnFe sample (450 s/900 °C), can reach some microns. When the thicker oxide layer is combined with typical fluctuations in the surface topography, the signal of Al is collected

from a relatively broad range with respect to the measuring depth. That has most likely caused the broadening of the Al peak. It can be assumed that Al originating from the steel (~0.03 wt %) does not contribute to the surface reactions or measured GDOES profiles, as it is not typically present in solution.

3.3. Crystal structures and morphology

Crystal structures and morphologies of die-quenched samples were analysed with EBSD. Band contrast (BC) and inverse pole figure (IPF) maps of representative 22MnB5-ZnFe and 34MnB5-Zn samples are presented in Fig. 8.

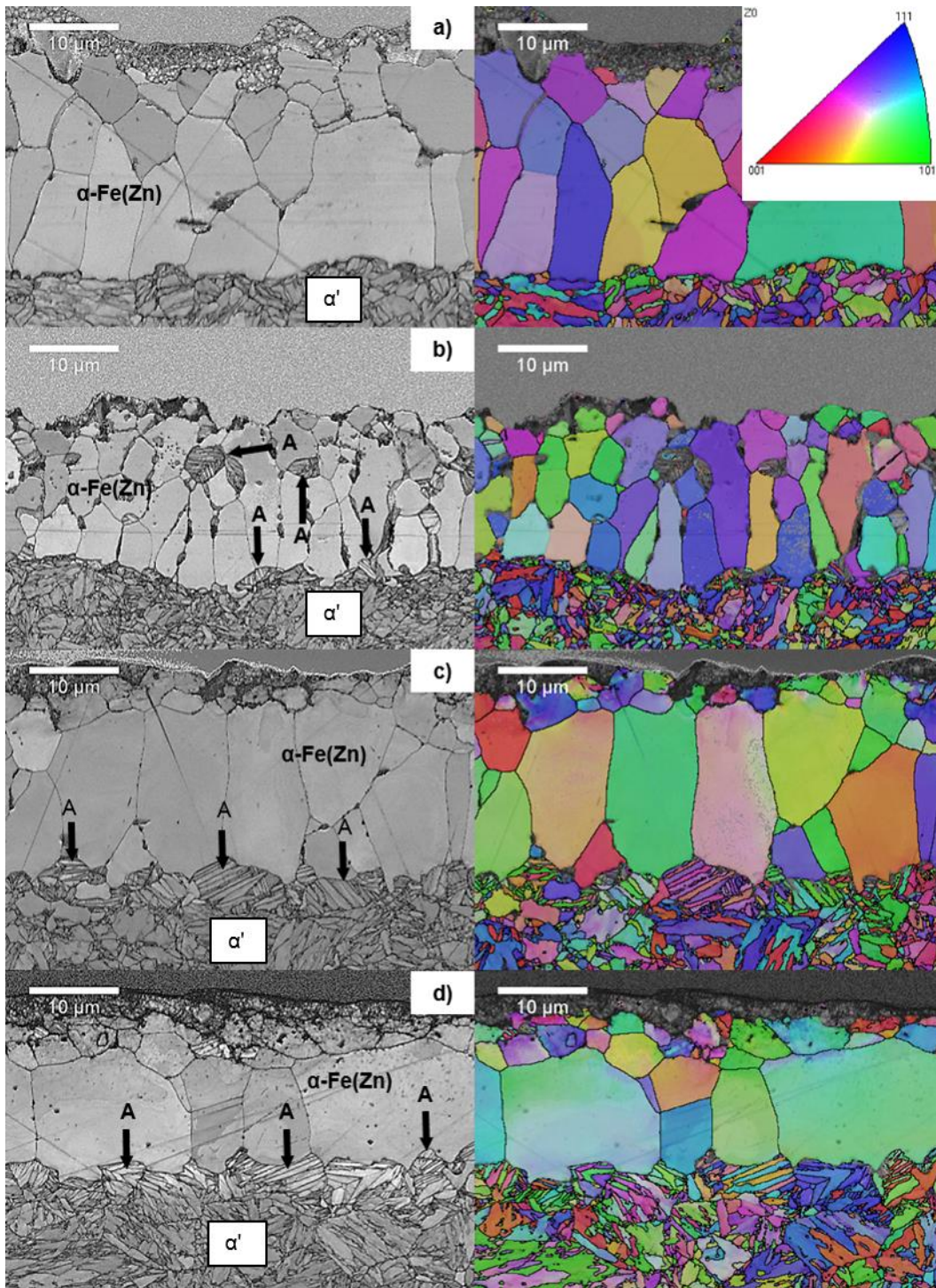


Fig. 8. Band contrast (left column) and inverse pole figure maps (right column) for; a) 22MnB5-ZnFe annealed for 450 s at 900 °C; b) 34MnB5-Zn annealed for 170 s at 880 °C; c) 34MnB5-Zn annealed for 470 s at 880 °C; d) 34MnB5-Zn annealed for 430 s at 930 °C. In IPF maps, the crystal structure of the regions of A has been for the most part identified as body centered cubic

(BCC) Fe similarly to ferritic α -Fe(Zn) and martensitic α' . (For interpretation of the references to colour in this figure legend, the reader is referred to the web version of this article).

As can be seen in Fig. 8, the areas corresponding to the micro constituents of A are body centered cubic (BCC) Fe by crystal structure. Therefore, the crystal structure is similar to the α -Fe(Zn) and α' . However, the morphology is clearly different to the ferritic α -Fe(Zn) that is present in the upper parts of the coating. Instead, the regions of A are seen as emerged into the steel and show similar type of morphology together with the martensitic base steel. However, the morphology of A resembles more preferably plate-like morphology than typical morphology of lath martensite as present little below in the base steel. The EBSD software has not been able to index all the finest crystals of the A, especially in case of short annealing cycle of 170 s/880 °C. Whereas only few crystals from the islands of A has been successfully indexed (Fig. 8b), the crystals from the regions of A, formed beneath α -Fe(Zn), have been indexed almost completely (Figs. 8c and 8d). In the case of 22MnB5-ZnFe (Fig. 8a), the EBSD was not able to distinguish any regions of A below the α -Fe(Zn) with the used magnification.

Selected samples were further analyzed in detail by means of high resolution (S)TEM. The typical outcomes of the TEM analysis are presented in Fig. 9.

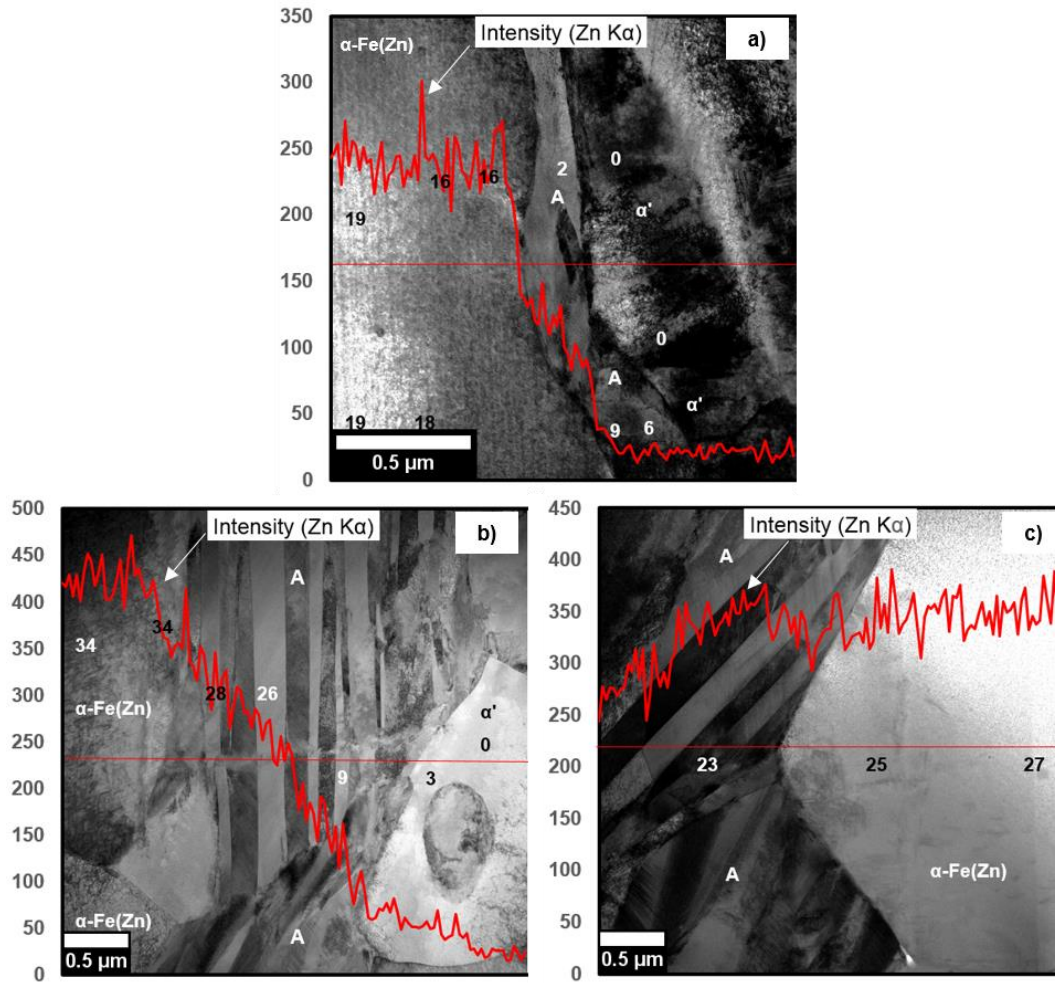


Fig. 9. STEM bright field (BF) images observed from the interface regions of the die-quenched samples of; a) 22MnB5-ZnFe (450 s/900 °C); b) 34MnB5-Zn (170 s at 880 °C); c) 34MnB5-Zn (470 s at 880 °C). STEM-EDS intensity curves of ZnK α are superimposed on BF images and EDS point analysis results are marked with numbers (Zn wt-%). Please note slightly larger magnification in a).

Fig. 9a implies that an extremely narrow layer of A can be identified also in the 22MnB5-ZnFe sample. This layer was not distinguishable in the EBSD map of the corresponding sample (Fig. 8a). As can be seen in Figs. 9b and 9c, the micro constituents of A are much better identifiable in the 34MnB5-Zn samples as also noticed with EBSD (Figs. 8b-d). The superimposed intensity

curves indicate that there exists clear transitions in Zn content when crossing the different regions. It can be seen that there is a relatively sharp drop in the Zn content when the interface between A and martensitic base steel α' is crossed (Figs. 9a and 9b). In the analyzed 22MnB5-ZnFe (Fig. 9a), there is also a sharp drop when crossing the interface between α -Fe(Zn) and A. However, there do not seem to be equally sharp drop in the Zn content when the α -Fe(Zn)/A interface is crossed in the 34MnB5-Zn samples (Figs. 9b and 9c). Furthermore, there is evidently an intensity gradient within the layer A, and thus it is difficult to determine the average Zn content for those regions. The Zn contents measured from the micro constituents of A are at maximum 9 wt-% in the presented 22MnB5 sample (Fig. 9a) and 28 wt-% in the 34MnB5 sample (Fig. 9b), respectively. It is worth noting that these results are based on the EDS point analysis from the selected spatial areas.

Fig. 10 presents more detailed TEM analysis on the regions of A from the 34MnB5-Zn samples.

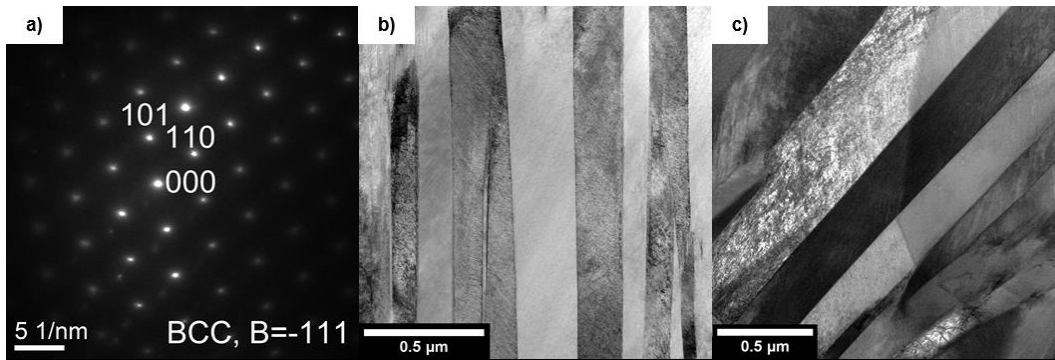


Fig. 10. a) Selected area diffraction pattern from regions of A showing BCC crystal structure. b) BF image showing plate-like martensitic morphology within layer A in 34MnB5-Zn (170 s/880 °C). c) BF image showing plate-like martensitic morphology within layer A in 34MnB5-Zn (470 s/880 °C). Please note slightly different magnification between b) and c).

Based on the selected area diffraction pattern (Fig. 10a) the regions of A represent BCC structure as noted also with EBSD (Fig. 8). Clear differences in the calculated atomic spacings were not observed between the other BCC structures of the samples, i.e., martensite of the steel and ferritic α -Fe(Zn). As indicated for example in Figs. 9b and 10b, the morphology of A is most preferably martensitic. In the case of 22MnB5, the morphology of A is not significantly different from the lath martensite of the steel (Fig. 9a). In turn, in the 34MnB5 samples (Figs. 10b and 10c), the morphology is not typical to lath martensite, but instead, resembles more plate-like martensite with extremely sharp crystal boundaries. The results are consistent with the crystal structures shown earlier in EBSD maps (Figs. 8a-d).

4. Discussion

4.1. Behavior of Zn and ZnFe coated 22MnB5

In general, the observed formation of the phase structures of Zn and ZnFe coated 22MnB5 are in line with earlier findings reported for example in [5] and [4], respectively. However, the present results propose a new insight into the phase structure formation as a result of annealing and subsequent die-quenching typical to the direct press hardening process. An interesting region designated as A was identified (Figs. 2d, 2g, and 2h). There exists some findings that support our observations suggesting the presence of a phenomenon that has not been completely discovered earlier. Kondratiuk et al. [5] analyzed Zn coated 22MnB5, annealed for 300 s at 880 °C, and noticed contrast differences in the lowest parts of the coating. However, the properties or composition of that layer were not discussed further and have not been addressed either in other studies. Janik et al. [9,22], in turn, discussed that the lowermost layer of the α -Fe(Zn) can be

transformed into austenite when annealed at 900 °C. Nevertheless, no clear evidence of the martensitic micro constituents containing Zn were identified from the die-quenched samples.

Based on present observations, the regions designated as A showed most preferably martensitic morphology and contained significant amount of Zn, for example 2-9 wt-% in the area presented in Fig. 9a. Considering the results of thermodynamic calculations (Fig. 1), it can be suggested that a small amount of martensitic micro constituents containing Zn, i.e., α' -Fe(Zn) are formed when Zn and ZnFe coated 22MnB5 are subjected to the direct press hardening process. The findings presented by Kondratiuk et al. [5] support our conclusion. The scientists analysed ZnNi coated 22MnB5 steel, annealed for 300 s at 880 °C, and identified unknown phase constituents from the coating after die-quenching. The unknown phase was formed mainly in the vicinity of steel/coating interface. However, the EDS mapping did not reveal compositional differences between the unknown phase and α -Fe(Zn) with a chemical composition of 3 wt-% Ni, 26 wt-% Zn, and 71 wt-%. Kondratiuk et al. [5] suggested that the unknown phase was most likely martensitic due to high hardness. Furthermore, the presence of Ni being a strong austenite stabilizer could stabilize austenitic phase with relatively high Zn content, and thus enable martensite transformation. Since the unknown phase was formed in the lowermost parts of the coating, the contribution of C and successive martensite formation can be assumed to be very likely. Thus, we suggest that the only significant difference in the chemical compositions between the unknown phase and α -Fe(Zn) was the C content that cannot be accurately identified with conventional SEM-EDS analysis.

According to the presented thermodynamic calculations (Fig. 1), the carbon originating from steel has a crucial effect in Fe-Zn phase equilibrium: the presence of C enables the stability of

austenitic solid solution of γ -Fe(Zn) at typical annealing temperatures around 900 °C. In 22MnB5 steels, the role of Mn, being also a strong austenite stabilizer, is also worth considering. It can be evaluated that the measured Mn contents, approximately 1 wt-% (Fig. 6), can also promote the stabilization of the γ -Fe(Zn) in the vicinity of the steel/coating interface as the Zn of the coating is mixed with the steel during annealing. The phase diagram of the 22MnB5-Zn system (0.23 wt-% C, 1.2 wt-% Mn, 0.2 wt-% Si, 0.2 wt-% Cr, 0.04 wt-% Al) presented by Janik et al. [22] can be used to evaluate the stabilizing effect of other alloying elements. In the 22MnB5-Zn system calculated in [22] the maximum solubility of Zn in austenite is 13 wt-% at 900 °C. As calculated in the present study, the maximum solubility of Zn with the corresponding C content of 0.23 wt-% is only about 7.5 wt-%. Regarding the difference of 13 wt-% - 7.5 wt-%, the aggregate stabilizing effect of the other alloying elements of 22MnB5 steel is 5.5 wt-%. Since the measured amounts of these elements are comparable (Table 1), and do not either show significant differences near steel/coating interface (Fig. 7), the diagram calculated in [22] can be satisfactorily used to evaluate the aggregate effect of Mn, Cr, Si, and Al also in the present study.

The aggregate influence of Mn, Cr, Si, and Al, i.e., 5.5 wt-%, can be combined with the stabilizing effect of the C contents that were measured in the present study. In 22MnB5 steels, approximately 0.25 wt-% C was present near steel/coating interface. This gives 8 wt-% Zn as indicated in Fig. 1b. Using the above-discussed method, the maximum solubility of Zn in austenite at 900 °C would be 5.5 wt-% (other elements) + 8 wt-% (carbon), which makes approximately 14 wt-% in total. This calculation means that γ -Fe(Zn) could be stabilized within the regions of the inter-diffusion layer containing no more than 14 wt-% of Zn. The estimated outcome gives a relatively good match with the measured values (Fig. 9a), since the Zn contents measured immediately above the α' -Fe(Zn)/ α -Fe(Zn) interface were 16 wt-%. Only 0.2-0.3 μ m

away, i.e., at slightly higher position, the measured Zn content was around 20 wt-%. Janik et al. [9] reported very similar results for ZnFe coated 22MnB5 annealed around 900 °C for different times.

The visual analysis of the 22MnB5-ZnFe samples (Fig. 2) showed no clear increase in amount of α' -Fe(Zn) between the samples that were annealed for different times, i.e., 180 s and 450 s at 900 °C. This means that in both cases, there has existed only a thin layer in which the thermodynamic requirements for the stabilization of the γ -Fe(Zn) has been fulfilled. Based on the TEM-EDS analysis (Fig. 9a) there is a steep Zn gradient from 20 wt-% to zero within a narrow region of only 1 μ m in thickness. Thus, the region having suitably low Zn content and high enough C content for stabilizing the γ -Fe(Zn) is narrow even in the case of prolonged annealing times at 900 °C. To support our results, Janik et al. [22] reported that the Zn content of the lowermost parts of α -Fe(Zn) is insensitive to annealing time, i.e., the study shows that there do not exist significant differences in Zn content after annealing for 300 and 600 s at 900 °C. Hence, the Zn content of approximately 20 wt-% can be considered as an equilibrium concentration of the lowermost parts of the α -Fe(Zn) layer. Also this conclusion explains the negligible effect of the increased annealing time in the 22MnB5-ZnFe samples. Consequently, also the practical significance of the observed phenomenon can be seen as low in Zn and ZnFe coated 22MnB5 steels.

4.2. Behavior of Zn and ZnFe coated 34MnB5

The investigated 34MnB5 grades exhibited clearly stronger formation of the regions designated as A; actually an uniform layer was formed in the vicinity of the steel/coating interface (Fig. 3).

Based on the observed morphology (Figs. 7-9), XRD results (Fig. 4), micro hardness measurements (Fig. 5), and conclusions regarding the behavior of 22MnB5 grades (section 4.1), the regions of A must be martensitic micro constituents of α' -Fe(Zn) also in 34MnB5 steels. The thermodynamic calculations (Fig. 1) suggested that higher C content stabilizes γ -Fe(Zn) with higher Zn contents, and thus the stronger formation of α' -Fe(Zn) can be understood.

In the case of 34MnB5-Zn, the Zn contents of α' -Fe(Zn) measured with SEM-EDS were 23-25 wt-% (Fig. 6). TEM-EDS analysis supported these results (Figs. 9b and 9c), but the higher spatial resolution gave a broader range of 9-28 wt-%. Since there is a compositional gradient within α' -Fe(Zn) layer, it is difficult to give a good estimation of the average Zn content. The amount of other alloying elements (Mn, Cr, Si, and Al) is practically the same in both 22MnB5 and 34MnB5 (Table 1), and their influence on the austenite stability can be assumed to be comparable. Therefore, the earlier estimated outcome of other alloying elements, i.e., 5.5 wt-% can be combined with the stabilizing effect resulting from the higher average C contents of 0.50 wt-%. Those values were measured from the regions near the steel/coating interface for 34MnB5 samples (Figs. 7c and 7d). The maximum Zn content with the C content of 0.50 wt-% is 14 wt-% at 900 °C (Fig. 1a). When using the earlier described calculation procedure, the estimated maximum Zn content of the γ -Fe(Zn) phase would be around 20 wt-% (5.5 wt-% + 14 wt-%). However, also clearly higher Zn values, e.g. 23-28 wt %, were measured from the regions of α' -Fe(Zn) that were present in samples annealed for 170 s and 470 s at 880 °C (Figs. 8b and 8c). Further discussions are needed to understand this discrepancy.

The observed discrepancy between thermodynamic calculations and measured Zn contents can be caused by several factors. To begin with, the presented GDOES results (Fig. 7) give only

approximate values from relatively large analyzing areas due to relatively poor spatial resolution of the method. Most importantly, the diagrams presented in Fig. 1 represent the equilibrium state of the systems. In particular, short annealing cycles with a relatively fast heating rates result that the equilibrium state cannot be attained. This is the case for example in the 34MnB5-Zn sample annealed for 170 s at 880 °C (Fig. 9b) for which the maximum temperature of 850 °C was reached. Therefore, the exceptionally high Zn contents of 28 wt-% measured near α -Fe(Zn) layer may be influenced by the metastability of the system. It can be deduced that the prolonged annealing time of 470 s is at least closer to the equilibrium state, and thus resulted in the decreased maximum values of around 23-24 wt-% Zn within α' -Fe(Zn) (Fig. 8c). This value gives better match with the calculated/evaluated threshold value of 20 wt-%.

According to the presented phase structures and EDS maps of 34MnB5 samples (Fig. 6), the thickness of the α' -Fe(Zn) layer increased significantly at the expense of the α -Fe(Zn) with increasing annealing time and temperature. Earlier studies [9,19] have pointed out that longer annealing time leads to the constant decrease in the Zn content of the α -Fe(Zn) phase on average. This result has been confirmed even though the Zn content of the lowermost parts of the α -Fe(Zn) layer are negligible with respect to annealing time as discussed in section 4.1. Based on the present results, the higher annealing temperature increases the solubility of Zn in austenite in the examined temperature range of 880-930 °C (Figs. 1c and 1d). Consequently, a larger amount of γ -Fe(Zn) is stabilized and finally transformed into α' -Fe(Zn) when longer annealing times and higher annealing temperatures are applied. In the case of 34MnB5, the maximum solubility of Zn in γ -Fe(Zn) may exceed the typical equilibrium value of the lowermost parts of α -Fe(Zn) being around 20 wt-%. This explains why significantly thicker α' -Fe(Zn) layer is formed in 34MnB5 grades as a function of the extended annealing time. Considering the kinetics and earlier

mentioned metastability, it is very likely that C partitions from α -Fe(Zn) to the austenite during the inter-diffusion process and allows the Zn content of the γ -Fe(Zn) increase without destabilizing the γ -Fe(Zn). This type of kinetic stabilization of the γ -Fe(Zn) could actually explain exceptionally high Zn contents in the γ -Fe(Zn) when annealed for short times.

It was shown (Fig. 3d) that the α' -Fe(Zn) layer can reach a thickness of approximately 5 μm within the typical annealing parameters. Therefore, it is meaningful to discuss the practical significance of this phenomenon in zinc-coated 34MnB5 steels. Simple hardness measurements of the α' -Fe(Zn) layer (Fig. 5) indicated that martensitic micro constituents α' -Fe(Zn) are harder than the ferritic α -Fe(Zn) phase of the coating. Regarding the observed morphological differences (Figs. 9c and 9d) the result is more than reasonable. However, the size of hardness indentation marks (Fig. 5) imply that the hardness values of the α' -Fe(Zn) are close to the lath martensite of the base steel. The GDOES measurement of the corresponding 34MnB5 sample (Fig. 7d) indicated that there is a peak in C content near steel/coating interface. However, due to nature of the GDOES method, the higher C content of the α' -Fe(Zn) cannot be fully confirmed. Hence, the different morphology between α' -Fe(Zn) and lath martensite of the base steel (Fig. 8) can be thought to be caused by high Zn content instead of significant differences in C contents. Regardless of the hardness values, the observed plate-like morphology of the α' -Fe(Zn) layer is an indication of the brittleness [29]. Still, more detailed investigations on the role of α' -Fe(Zn) layer in the mechanical behavior of press hardened 34MnB5 steels would be needed. The present study suggests that the observed phenomenon needs to be taken into account, but further analysis are left outside of the scope of this work.

Another interesting finding mentioned in section 3.1., was the formation of the islands of A in the upper parts of the coating. That phenomenon was observed only for 34MnB5-Zn samples annealed for relatively short times, e.g., 170 s at 880 °C. The GDOES profile of the corresponding 34MnB5-Zn sample (Fig. 7c), showed clearly higher C contents in the depths of 3-10 μm from the surface. The higher Mn content cannot be confirmed on the basis of the GDOES curve, but EDS point analysis (Fig. 6a, middle) gave Mn contents around 1 wt-% from the islands of A. These values are higher than typically measured from $\alpha\text{-Fe(Zn)}$ phase. Relatively high C and Mn contents and XRD results (Fig. 4) suggest that the islands are also martensitic micro constituents of $\alpha'\text{-Fe(Zn)}$. The presence of C in solid solution explains different etching depth between the islands of A and $\alpha\text{-Fe(Zn)}$ (Fig. 6a, middle). More interestingly, the islands were not observed in any 34MnB5-ZnFe samples. In order to explain this behavior, physical properties of Zn and ZnFe coatings need to be considered. It is known that the conventional Zn coating has low thermal stability due to low melting point of pure Zn (420 °C), whereas the melting point of the ZnFe coating consisting of intermetallic Zn-Fe phases is higher [3,28]. Accordingly, Schachinger et al. [30] reported that the coating evolution of ZnFe coated 20MnB8 was more columnar by nature compared to Zn coated 22MnB5. Regarding this, it is likely that no liquid phase was present in the lowermost parts of the coating during the annealing phase of the ZnFe coated 34MnB5. The present results showing dissimilar behavior between Zn and ZnFe coated 34MnB5 support this observation. In addition, the phase structure of 34MnB5-ZnFe (Fig. 3e), indicates that the $\alpha\text{-Fe(Zn)}$ layer is relatively dense and uniform near the steel/coating interface. Therefore, it is likely that the liquid has not reacted with the steel in a similar way as in the case of Zn coating.

It is reasonable to believe that the observed difference in the behavior of 34MnB5-Zn and 34MnB5-ZnFe is caused by larger volume fraction of liquid phases when heating the conventional Zn coating. As seen in the optical micrograph of the 22MnB5-Zn sample (Fig. 2a), a majority of the coating has melted temporarily when reaching 820 °C. However, re-solidification of the coating has occurred through the formation of α -Fe(Zn) as the Fe content of the coating has increased (Fig. 2c). The amount of the Γ -ZnFe phase was small in the 34MnB5-Zn sample (Figs. 3a and Fig. 4), meaning that the re-solidification of the coating had proceeded quickly until reaching a temperature of 850 °C. In a general level, the mass of the Zn coating (50/50 g/m²) is relatively small, and thus the solidification of the coating could occur rapidly. Therefore, a valid explanation for the behavior of Zn coated 34MnB5 would be fast but short-term melting of the Zn coating that has occurred also in the regions touching the surface of the steel. Another issue to consider is the different Al content of Zn and ZnFe coatings. The higher Al content of the zinc bath is used when producing Zn coatings, since Al enhances the formation of so called inhibition layer that prevents the formation of brittle intermetallic Fe-Zn compounds [3]. Hence, the heating induces the breakdown of the inhibition layer in Zn coated steels, which occurs in a very uneven manner. This should also promote the melting of the lowermost parts of the Zn coating, in particular in the regions where Fe-Zn reactions are delayed. In the case of ZnFe coating, the inhibition layer does not exist in the galvanized state, i.e., in the initial state of the ZnFe coated PHS. In that case the direct contact between the liquid phase and the base steel is most likely prevented.

More explanations are still needed to understand the sequence of phase transformations occurring during the heating stage of the 34MnB5-Zn samples. Mörtlbauer et al. [17] reported that Γ -ZnFe transforms very rapidly into the mixture of α -Fe(Zn) and liquid when the temperature of 760-780

°C is attained during heating of Zn coated 22MnB5 steel. Simultaneously, a steel consisting initially of ferrite and cementite transforms into austenite. Based on this, it can be suggested that the C rich areas of the steel surface (cementite particles) provide the first nucleation sites for the γ -Fe. The locally high C content could allow the formation of γ -Fe(Zn) as the Zn diffuses towards steel. This process may result in exceptionally high C content in the γ -Fe(Zn) phase and would explain higher Zn contents compared to the equilibrium state. After that, the islands of the γ -Fe(Zn) with exceptionally high Zn content are separated from the γ -Fe(Zn) layer, but are still stabilized for a certain amount of time due to continuing C partitioning from the α -Fe(Zn). As indicated in the SEM-EDS point analysis results (Fig. 6), the Zn contents of the martensitic islands of A were as high as 36 wt-%. Hence, it is believed that the kinetic stabilization of γ -Fe(Zn) described above can enhance the observed behavior, since the diffusion rate of C is significantly higher compared to Zn. Finally, the martensitic islands are vanished as a result of the prolonged annealing (Figs. 3b and 3d) due to reduction in the local C contents and partitioning. As a conclusion, it can be suggested that the formation and presence of the α' -Fe(Zn) in the upper parts of the coating is insignificant phenomenon in practice. This is because ZnFe coatings are preferred in the direct press hardening of commercial PHS [31].

5. Conclusions

The following conclusions can be made based on the findings of the presents study:

- A new insight into the phase formation of Zn and ZnFe coated 22MnB5 steels was found regarding the typical heat treatment cycle of the direct press hardening process. Small regions of martensitic phase constituents α' -Fe(Zn) were identified near steel/coating

interface after die-quenching. However, the practical significance of this phenomenon is considered as low in 22MnB5 steels.

- A significantly stronger formation α' -Fe(Zn) was observed after die-quenching in Zn and ZnFe coated 34MnB5 steels. The α' -Fe(Zn) formed mainly as a continuous layer near steel/coating interface and was clearly emerged into the martensitic steel. The practical significance of a relatively thick α' -Fe(Zn) zone needs to be carefully considered.
- The differences between 22MnB5 and 34MnB5 can be explained with higher the C content of the 34MnB5. It seems evident that high C content of the 34MnB5 steel and simultaneous occurring partitioning of C from the α -Fe(Zn) to the γ -Fe(Zn) can effectively stabilize the γ -Fe(Zn) during the annealing/austenitization stage of the direct press hardening process.
- In the case of Zn coated 34MnB5, the presence of martensitic islands of α' -Fe(Zn) was observed also in the upper parts of the coating. It is suggested that a short term melting of the Zn coating and simultaneously occurring austenite formation in steel enable the following reactions: C rich areas of the steel surface (cementite particles) provide nucleation sites for γ -Fe and locally high C content allows the formation of γ -Fe(Zn) as the Zn diffuses towards the steel. This process can result in exceptionally high C content in the γ -Fe(Zn) phase and would explain higher Zn contents compared to the equilibrium state. After that, the islands of the γ -Fe(Zn) are separated from the steel/coating interface, but are still stabilized with high Zn contents for a certain amount of time due to continuing C partitioning from the α -Fe(Zn) phase.
- The α' -Fe(Zn) layer formed in 34MnB5 showed plate-like morphology, but comparable micro hardness values with the martensite of the base steel. The formation of α' -Fe(Zn) with a relatively high Zn content needs to be considered from the mechanical behavior

point of view. Therefore, the formation of α' -Fe(Zn) layer needs to be taken into account in press hardening steels of 34MnB5 type.

Acknowledgements

We acknowledge the provision of facilities and technical support by Aalto University at OtaNano - Nanomicroscopy Center (Aalto-NMC). Hans Magnusson (Swerea KIMABB, Sweden) and Ulrika Borggren (SSAB Europe, Sweden) are gratefully acknowledged for carrying out thermodynamic calculations with Thermo-Calc®. SSAB Europe (Hämeenlinna, Finland) is acknowledged for providing facilities for GDOES measurements. This study was financially supported by the Finnish Funding Agency for Technology and Innovation (Tekes) in the Breakthrough Steels and Applications Program of the Finnish Metals and Engineering Competence Cluster (FIMECC Ltd), which is gratefully acknowledged. The author wants to thank Tampere University of Technology (TUT's Graduate School), Emil Aaltonen Foundation, and Finnish Foundation for Technology Promotion for financial support.

Reference List

- [1] G. Hensen, W. Melfo, S. Chen, R. Bleeker, W. Verloop, Developing Zinc Coated Boron Steel: Balancing Microcrack Performance and Corrosion Protection, in: M. Oldenburg, P. Prakash, K. Steinhoff, (Eds.), Proc. 4th International Conference on Hot Sheet Metal Forming of High-Performance Steel, Luleå, 2013, pp. 463-470.
- [2] J. Singh, J. Hall, J. Jason, Challenges with Zinc-Coated Press Hardened Steels, in: M. Oldenburg, P. Prakash, K. Steinhoff, (Eds.), Proc. 4th International Conference on Hot Sheet Metal Forming of High-Performance Steel, Luleå, 2013, pp. 433-444.
- [3] A.R. Marder, The Metallurgy of Zinc-coated Steel, Prog. Mater. Sci. 45 (2000) 191-271.
- [4] M. Van Genderen, W. Verloop, J. Loiseaux, G. Hensen, Zinc-Coated Boron Steel, ZnX[®]: Direct Hot Forming for Automotive Applications, in: M. Oldenburg, K. Steinhoff, P. Prakash (Eds.), Proc. 3rd International Conference on Hot Sheet Metal Forming of High-Performance Steel, Kassel, 2011, pp. 145-152.
- [5] J. Kondratiuk, P. Kuhn, E. Labrenz, C. Bischoff, Zinc Coatings for Hot Sheet Metal Forming: Comparison of Phase Evolution and Microstructure during Heat Treatment, Surf. Coat. Tech. 205 (2011) 4141-4153.
- [6] J. Kondratiuk, P. Kuhn, M. Köyer, M. Meurer, J. Horstmann, F.-. Lenze, A New Coating Solution for Press Forming, in: M. Oldenburg, K. Steinhoff, P. Prakash (Eds.), Proc. 3rd International Conference on Hot Sheet Metal Forming of High-Performance Steel, Kassel, 2011, pp. 1-10.
- [7] M. Köyer, J. Banik, S. Graff, J.F. Lenze, G. Parma, S. Sikora, Zinc Alloy Coating for the Hot Forming Process, in: M. Oldenburg, P. Prakash, K. Steinhoff, (Eds.), Proc. 4th International Conference on Hot Sheet Metal Forming of High-Performance Steel, Luleå, 2013, pp. 363-370.
- [8] K. Mori, P.F. Bariani, B.-. Behrens, A. Brosius, S. Bruschi, T. Maeno, M. Merklein, J. Yanagimoto, Hot stamping of ultra-high strength steel parts, CIRP Ann.-Manuf. Techn. 66 (2) (2017) 755-777.
- [9] V. Janik, P. Beentjes, D. Norman, G. Hensen, S. Seetharaman, Role of Heating Conditions on the Microcrack Formation in Zinc Coated 22MnB5, in: Proc. Materials Science and Technology (MS&T), Pittsburg, 2014.
- [10] P.B. Burton, P. Perrot, Phase diagram of binary iron alloys, American Society for Metals, Metals Park, OH, 1993, pp. 459-466.
- [11] J. Faderl, S. Kolnberger, T. Kurz, G. Luckeneder, T. Manzenreiter, M. Rosner, PHS-Ultraform - Continuous Galvanizing meets Press-Hardening, in: M. Oldenburg, K. Steinhoff, P. Prakash (Eds.), Proc. 3rd International Conference on Hot Sheet Metal Forming of High-Performance Steel, Luleå, 2009, pp. 283-291.

- [12] K. Akioka, T. Nishibata, K. Imai, T. Takayama, M. Nakata, H. Fujimoto, N. Kojima, M. Matsumoto, Layer Structure and Properties of Galvannealed Steel Sheet after Hot Stamping, in: Proc. 8th International Conference of Zinc and Zinc Alloy Coated Sheet (Galvatech), Genova, 2011.
- [13] C. Lee, D. Fan, S. Lee, I. Sohn, B. De Cooman, Galvanized Coating Evolution during Hot Stamping, in: Proc. 8th International Conference of Zinc and Zinc Alloy Coated Sheet (Galvatech), Genova, 2011.
- [14] C. Lee, D. Fan, I. Sohn, S.J. Lee, B. De Cooman, Liquid-Metal-Induced Embrittlement of Zn-Coated Hot Stamping Steel, Metall. Mater. Trans. A. 53 (2012) 5122-5127.
- [15] A. Ademaj, U. Weldig, K. Steinhoff, Phenomenological Thermo-Physical Approach on Process Monitoring in Hot Stamping of Coated Boron Steel, in: M. Oldenburg, P. Prakash, K. Steinhoff, (Eds.), Proc. 4th International Conference on Hot Sheet Metal Forming of High-Performance Steel, Luleå, 2013, pp. 239-248.
- [16] R. Autengruber, G. Luckeneder, S. Kolnberger, J. Faderl, A. Walter Hassel, Surface and Coating Analysis of Press-Hardened Hot-Dip Galvanized Steel Sheet, Steel Res. Int. 83 (2012) 1005-1011.
- [17] T. Mörtlbauer, S. Kolnberger, J. Faderl, XRD-measurements of Coating Formation of Hot-dip Galvanized Steel During Press Hardening, in: Proc. 10th International Conference of Zinc and Zinc Alloy Coated Sheet (Galvatech), Toronto, 2015, pp. 861-867.
- [18] D. Fan, B. De Cooman, State-of-the-Knowledge on Coating Systems for Hot Stamped Parts, Steel Res. Int. 83 (2012) 412-433.
- [19] H. Järvinen, S. Järn, E. Lepikko, M. Järvenpää, P. Peura, ZnFe Coated 22MnB5 Steels in Direct Press Hardening: the Relationships between Coating Structure and Process Parameters, Key Eng. Mat. 674 (2016) 331-336.
- [20] K. Imai, Y. Yoshikawa, T. Toki, K. Nishibata, M. Uematsu, T. Uchihara, T. Takayama, Properties of Hot Stamped Galvannealed Steel Sheet, SEAIISI quarterly 34 (2005) 47-53.
- [21] J. Faderl, R. Vehof, Press Hardening Steel (PHS): A New Coating and Process Technology, in: Proc. International Conference on SCT 2005, Wiesbaden, 2005, pp. 172-178.
- [22] V. Janik, Y. Lan, P. Beentjes, D. Norman, G. Hensen, S. Sridhar, Zn Diffusion and $\hat{\Gamma}$ -Fe(Zn) Layer Growth During Annealing of Zn-Coated B Steel, Metall. Mater. Trans. A. 47 (2016) 400-411.
- [23] A. Tokizawa, K. Yamamoto, Y. Takemoto, T. Senuma, Development of 2000MPa Class Hot Stamped Steel Components with Good Toughness and High Resistance against Delayed Fracture, in: M. Oldenburg, P. Prakash, K. Steinhoff, (Eds.), Proc. 4th International Conference on Hot Sheet Metal Forming of High-Performance Steel, Luleå, 2013, pp. 473-479.

- [24] T. Gerber, I. Heckelmann, N. Vives Diaz, F.-J. Lenze, Efforts in Expanding the Portfolio of Hot Forming Steel Material Concepts, in: M. Oldenburg, P. Prakash, K. Steinhoff, (Eds.), Proc. 4th International Conference on Hot Sheet Metal Forming of High-Performance Steel, Luleå, 2013, pp. 145-152.
- [25] H. Mohrbacher, Influence of Alloy Modifications and Microstructure on Properties and Crash Performance of Press Hardened Steel Components, in: M. Oldenburg, P. Prakash, K. Steinhoff, (Eds.), Proc. 6th International Conference on Hot Sheet Metal Forming of High-Performance Steel, Atlanta, 2017, pp. 213-220.
- [26] O.G. Kasatkin, B.B. Vinokur, V.L. Pilyushenko, Calculation models for determining the critical points of steel, *Met. Sci. Heat Treat.* 26 (1984) 27-31.
- [27] H. Järvinen, M. Isakov, T. Nyyssönen, M. Järvenpää, P. Peura, The effect of initial microstructure on the final properties of press hardened 22MnB5 steels, *Mater. Sci. Eng. A.* 676 (2016) 109-120.
- [28] X. Su, N. Tang, J.M. Toguri, Thermodynamic evaluation of the Fe–Zn system, *J. Alloy. Compd.* 325 (2001) 129-136.
- [29] G. Krauss, Martensite in steel: strength and structure, *Mater. Sci. Eng. A.* 273–275 (1999) 40-57.
- [30] E.D. Schachinger, S. Kolnberger, J. Faderl, Evolution of Phases and Formation of Oxides on Different Galvanized Hot Formed Steel Grades, in: M. Oldenburg, P. Prakash, K. Steinhoff, (Eds.), Proc. 6th International Conference on Hot Sheet Metal Forming of High-Performance Steel, Atlanta, 2017, pp. 111-119.
- [31] T. Kurz, P. Larour, J. Lackner, T. Steck, G. Jesner, Press-hardening of zinc coated steel – characterization of a new material for a new process, in: Proc. E. Till et al. (Ed.), Annual Conference of the International Deep Drawing Research Group (IDDRG 2016), Linz, 2016, pp. 414-427.

Table 1. Details and chemical compositions (wt-%) of the as-received test materials.

Steel	Sheet thickness	Coating weight (side/side)	C %	Si %	Mn %	Cr %	Al %	B %	A _{c3} (°C)
22MnB5-Zn	1.5 mm	50/50 g/m ²	0.24	0.26	1.18	0.20	0.033	0.0029	831
22MnB5-ZnFe	1.5 mm	70/70 g/m ²	0.23	0.26	1.24	0.21	0.029	0.0031	830
34MnB5-Zn	1.1 mm	50/50 g/m ²	0.35	0.26	1.30	0.15	0.033	0.0026	800
34MnB5-ZnFe	1.5 mm	70/70 g/m ²	0.35	0.25	1.32	0.15	0.033	0.0014	803

Table II. Parameters of the examined annealing cycles. The attained peak temperature of each cycle is expressed in the parenthesis.

Steel	880 °C: A _{c3} +30 s, A _{c3} +330 s	900 °C: total dwell times	930 °C: A _{c3} +330 s
22MnB5-Zn		180 s (820 °C), 450 s (900 °C)	
22MnB5-ZnFe		180 s (890 °C), 450 s (900 °C)	
34MnB5-Zn	170 s (850 °C), 470 s (880 °C)	180 s (890 °C), 450 s (900 °C)	430 s (930 °C)
34MnB5-ZnFe		180 s (890 °C), 450 s (900 °C)	

Fig. 1. a) Calculated Fe-Zn phase diagram. b) Maximum solubility of Zn in austenite (FCC_A1) at 900 °C as a function of C content. Isoplethal sections of the Fe-Zn-C system with C contents of; c) 0.25 wt-%; d) 0.50 wt-%. Designation BCC_A2 refers to the ferritic solid solution α -Fe(Zn).

Fig. 2. Optical micrographs of the die-quenched 22MnB5-Zn annealed for; a) 180 s; b) 450 s at 900 °C along with SEM (BSE) micrographs corresponding to; c) 180 s; d) 450 s. Optical micrographs of the die-quenched 22MnB5-ZnFe annealed for; e) 180 s; f) 450 s at 900 °C along with SEM (BSE) micrographs; g) 180 s; h) 450 s.

Fig. 3. Optical micrographs of the die-quenched 34MnB5-Zn annealed for; a) 180 s; b) 450 s at 900 °C along with SEM (BSE) micrographs corresponding to; c) 180 s; d) 450 s. Optical micrographs of the die-quenched 34MnB5-ZnFe annealed for; e) 180 s; f) 450 s at 900 °C along with SEM (BSE) micrographs; g) 180 s; h) 450 s.

Fig. 4. Results of the X-ray diffraction measurements for; a) 34MnB5-Zn annealed for 180 s; b) 450 s. The main intensity peaks of ZnO and α -Fe(Zn) are marked with asterisk.

Fig. 5. SEM image showing Vickers indentation marks (HV 0.5 g) in identified layers of a 34MnB5-Zn sample annealed for 430 s at 930 °C.

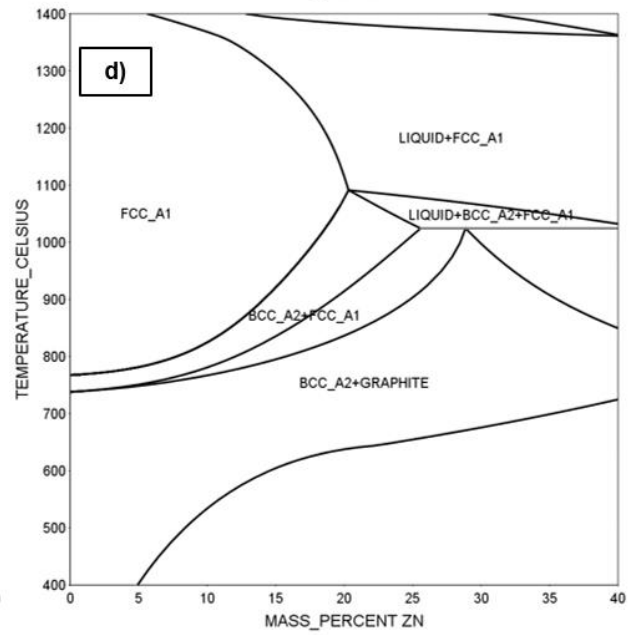
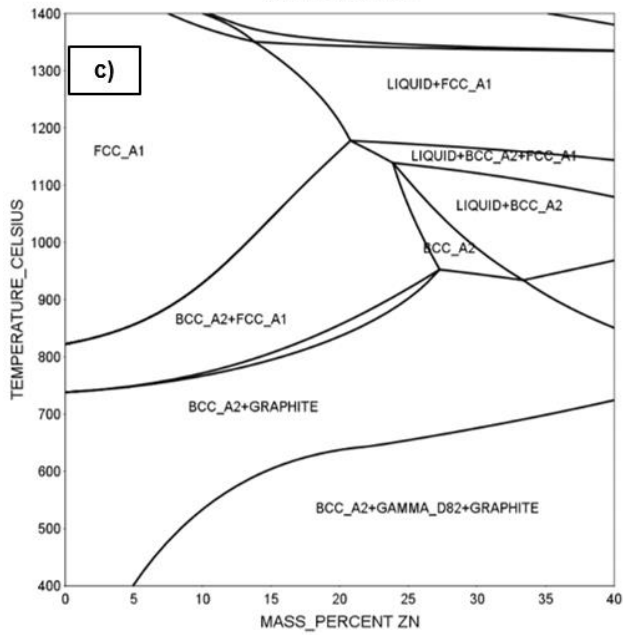
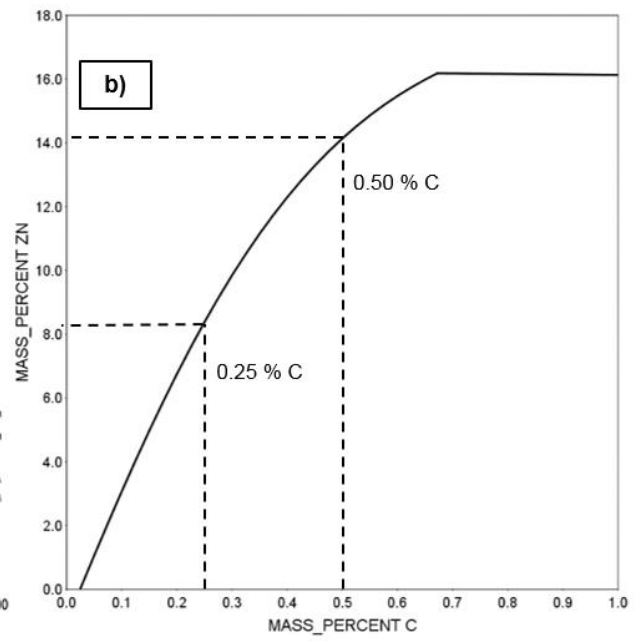
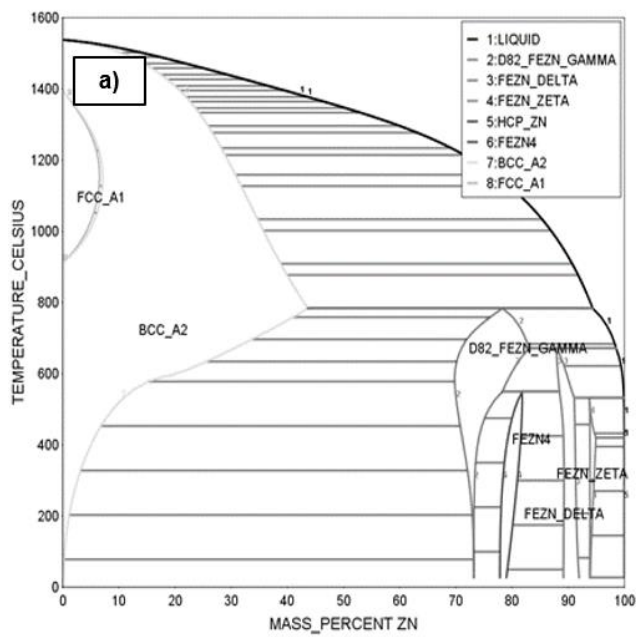
Fig. 6. BSE-images (left column), SE-images together with superimposed EDS point analysis results (Zn wt-%) (middle column), and EDS maps (ZnK α) (right column) for 34MnB5-Zn annealed for; a) 170 s at 880 °C; b) 470 s at 880 °C; c) 430 s at 930 °C.

Fig. 7. Elemental GDOES profiles for; a) 22MnB5-Zn (450 s/900 °C); b) 22MnB5-ZnFe (450 s/900 °C); c) 34MnB5-Zn (170 s/880 °C); d) 34MnB5-Zn (430 s/930 °C). The curves of other alloying elements are omitted for clarity. The steel/coating interface, originally defined according to the derivative curve of the Fe content, is marked with a dashed vertical line. The legend presented in a) is the same for all graphs. (For interpretation of the references to colour in this figure legend, the reader is referred to the web version of this article).

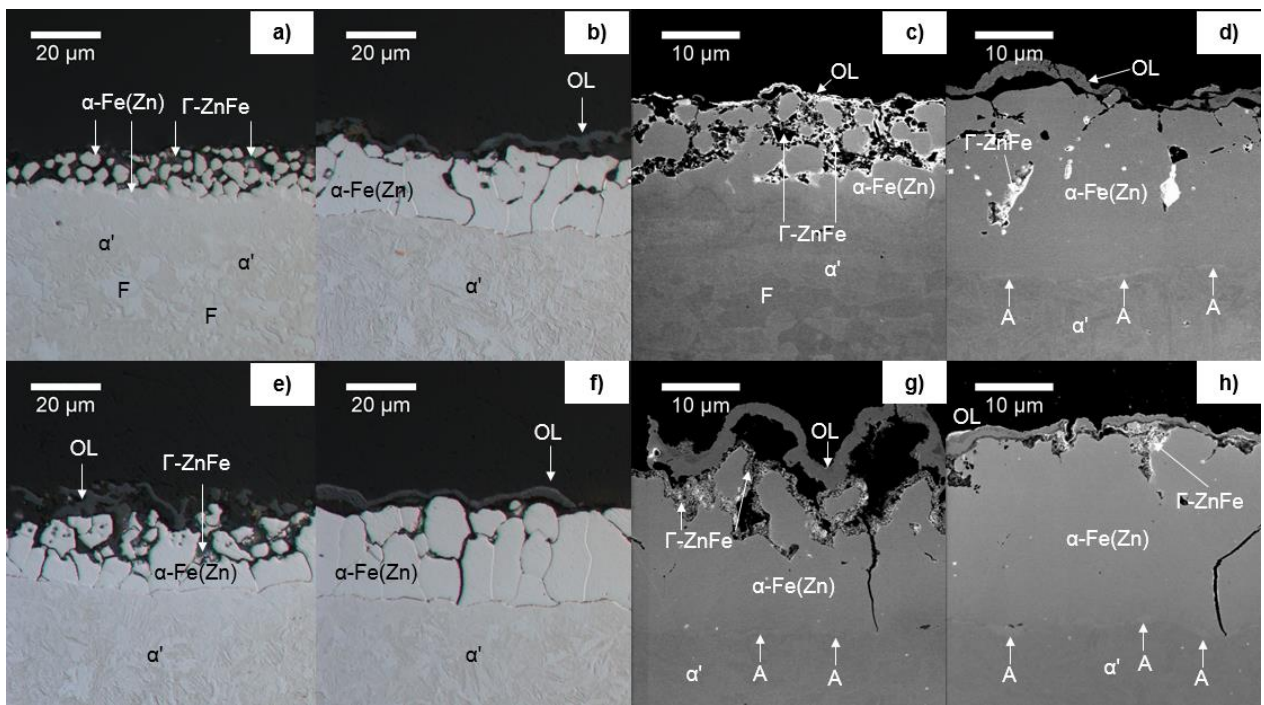
Fig. 8. Band contrast (left column) and inverse pole figure maps (right column) for; a) 22MnB5-ZnFe annealed for 450 s at 900 °C; b) 34MnB5-Zn annealed for 170 s at 880 °C; c) 34MnB5-Zn annealed for 470 s at 880 °C; d) 34MnB5-Zn annealed for 430 s at 930 °C. In IPF maps, the crystal structure of the regions of A has been for the most part identified as body centered cubic (BCC) Fe similarly to ferritic α -Fe(Zn) and martensitic α' . (For interpretation of the references to colour in this figure legend, the reader is referred to the web version of this article)

Fig. 9. STEM bright field (BF) images observed from the interface regions of the die-quenched samples of; a) 22MnB5-ZnFe (450 s/900 °C); b) 34MnB5-Zn (170 s at 880 °C); c) 34MnB5-Zn (470 s at 880 °C). STEM-EDS intensity curves of ZnK α are superimposed on BF images and EDS point analysis results are marked with numbers (Zn wt-%). Please note slightly larger magnification in a).

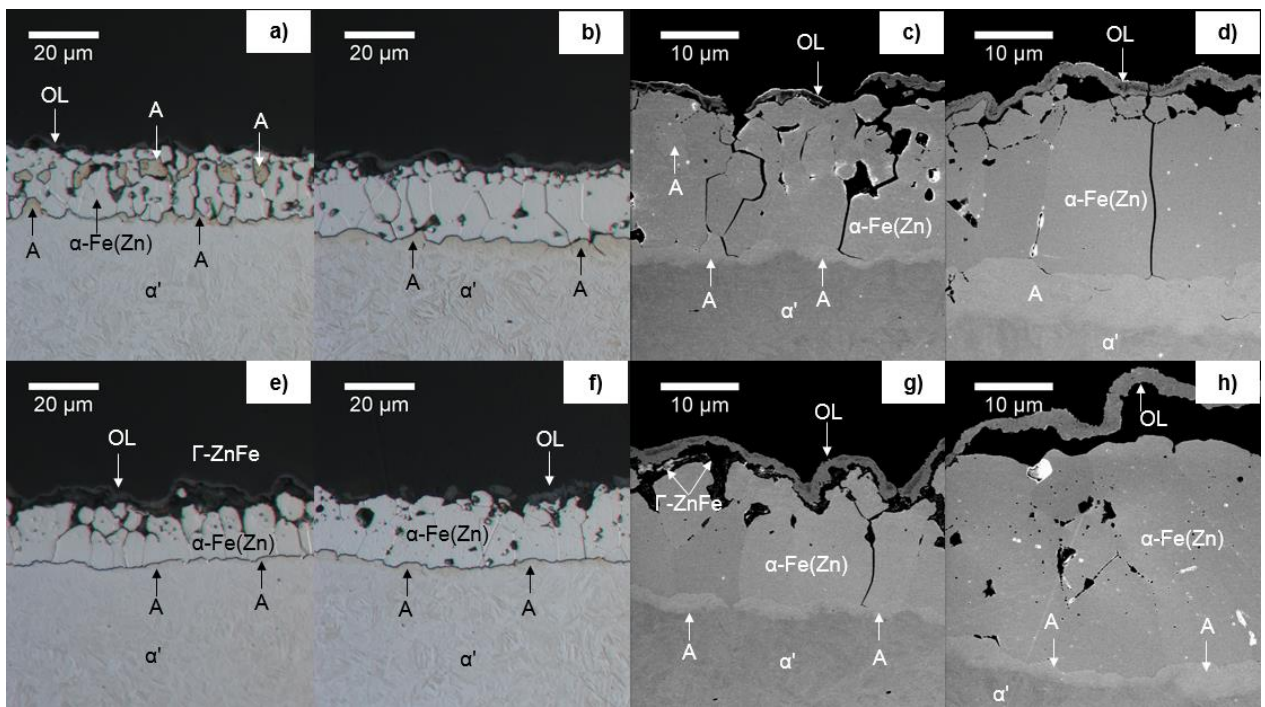
Fig. 10. a) Selected area diffraction pattern from regions of A showing BCC crystal structure. b) BF image showing plate-like martensitic morphology within layer A in 34MnB5-Zn (170 s/880 °C). c) BF image showing plate-like martensitic morphology within layer A in 34MnB5-Zn (470 s/880 °C). Please note slightly different magnification between b) and c).



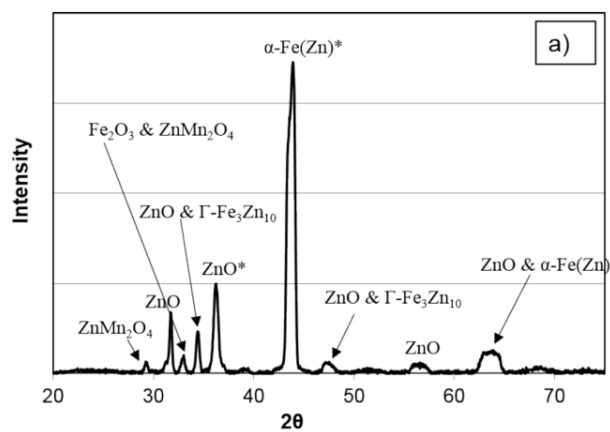
1



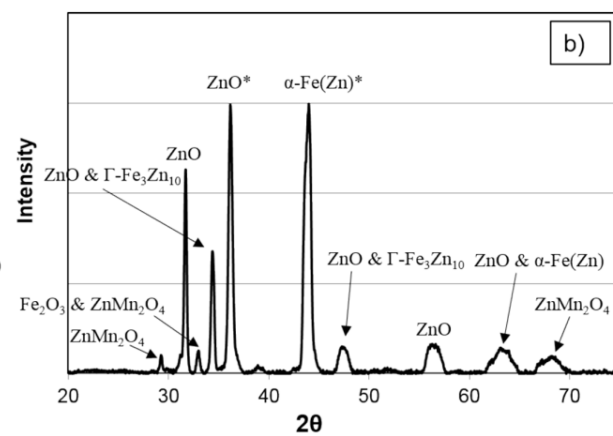
2

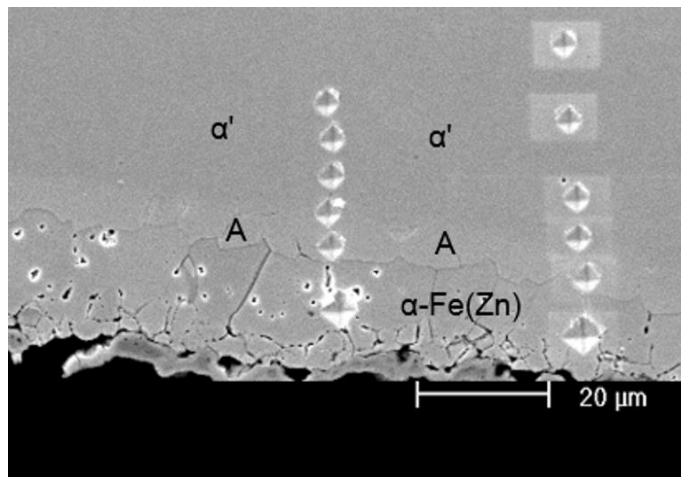


3

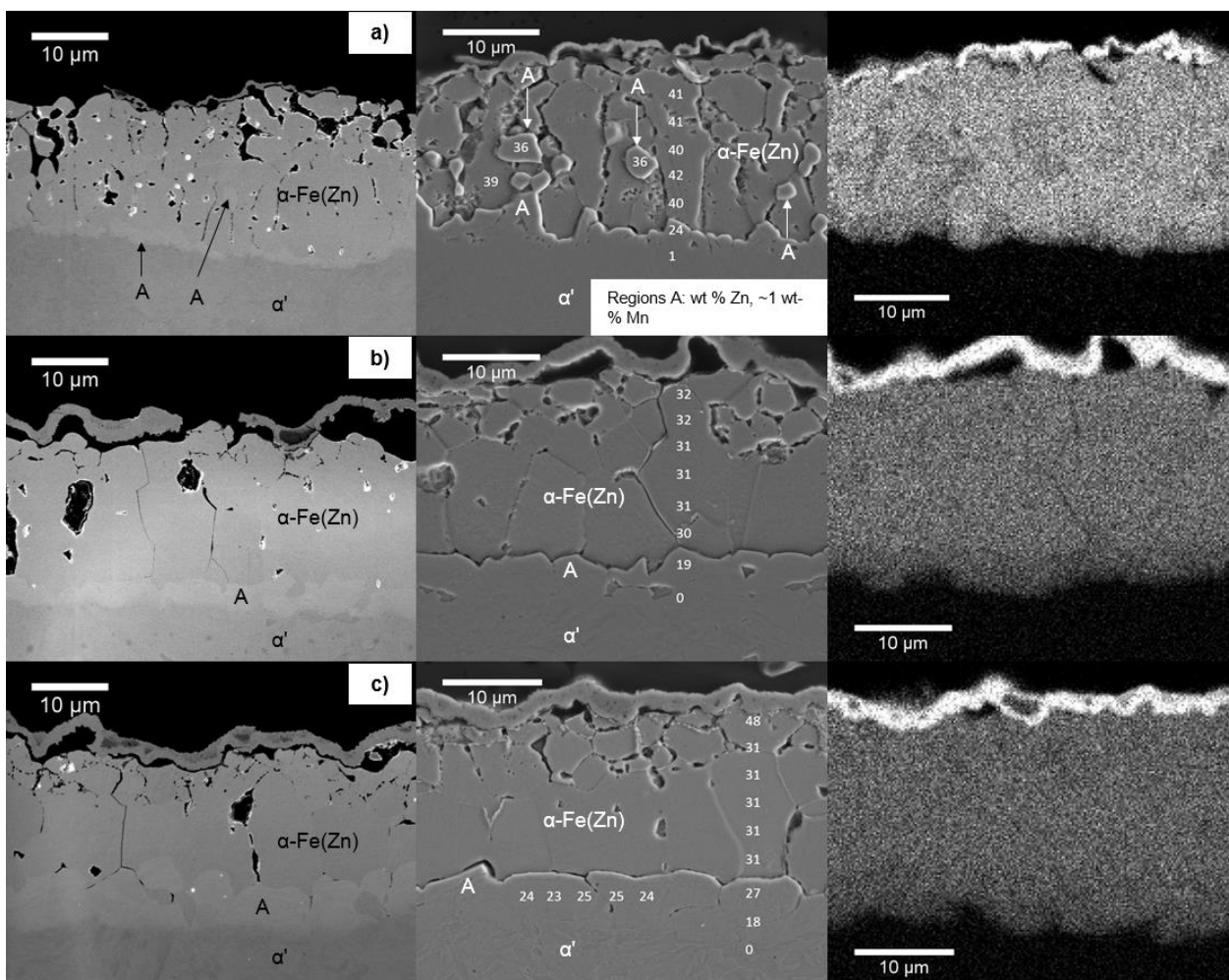


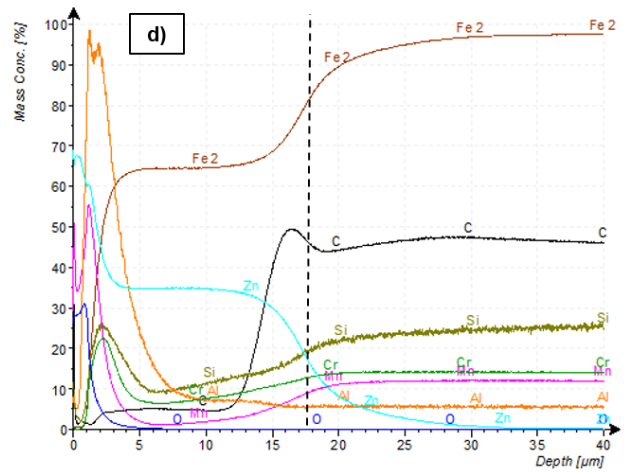
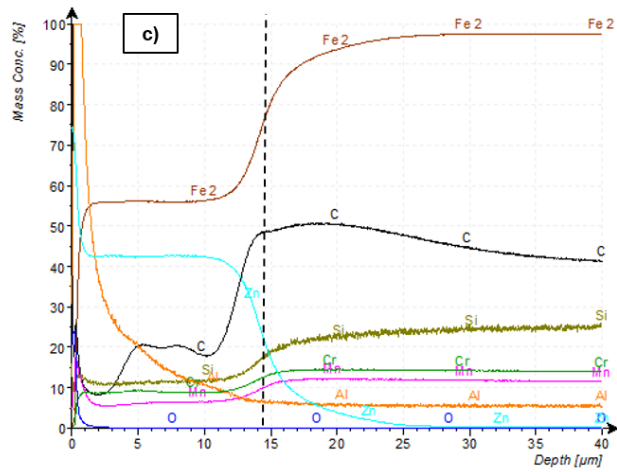
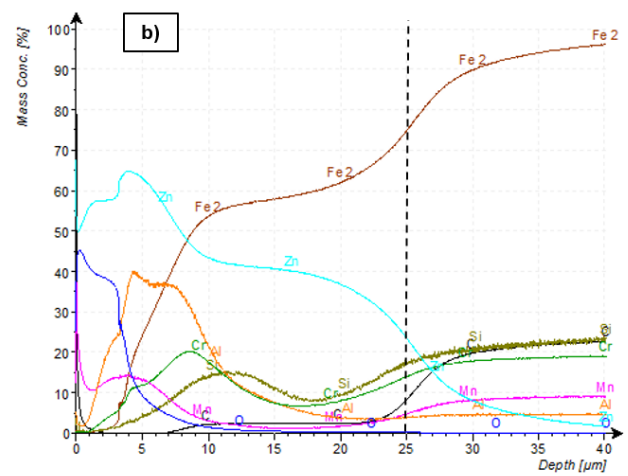
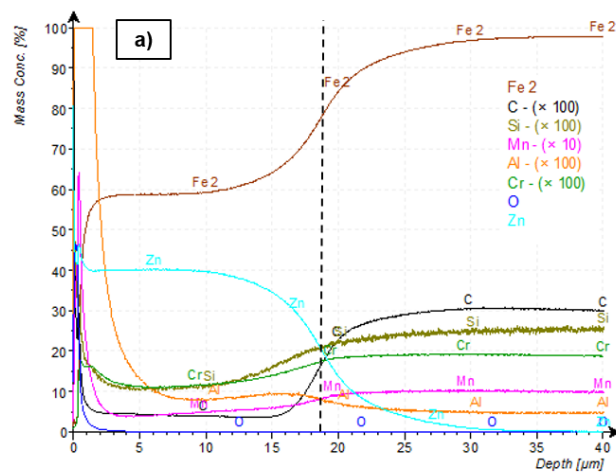
4

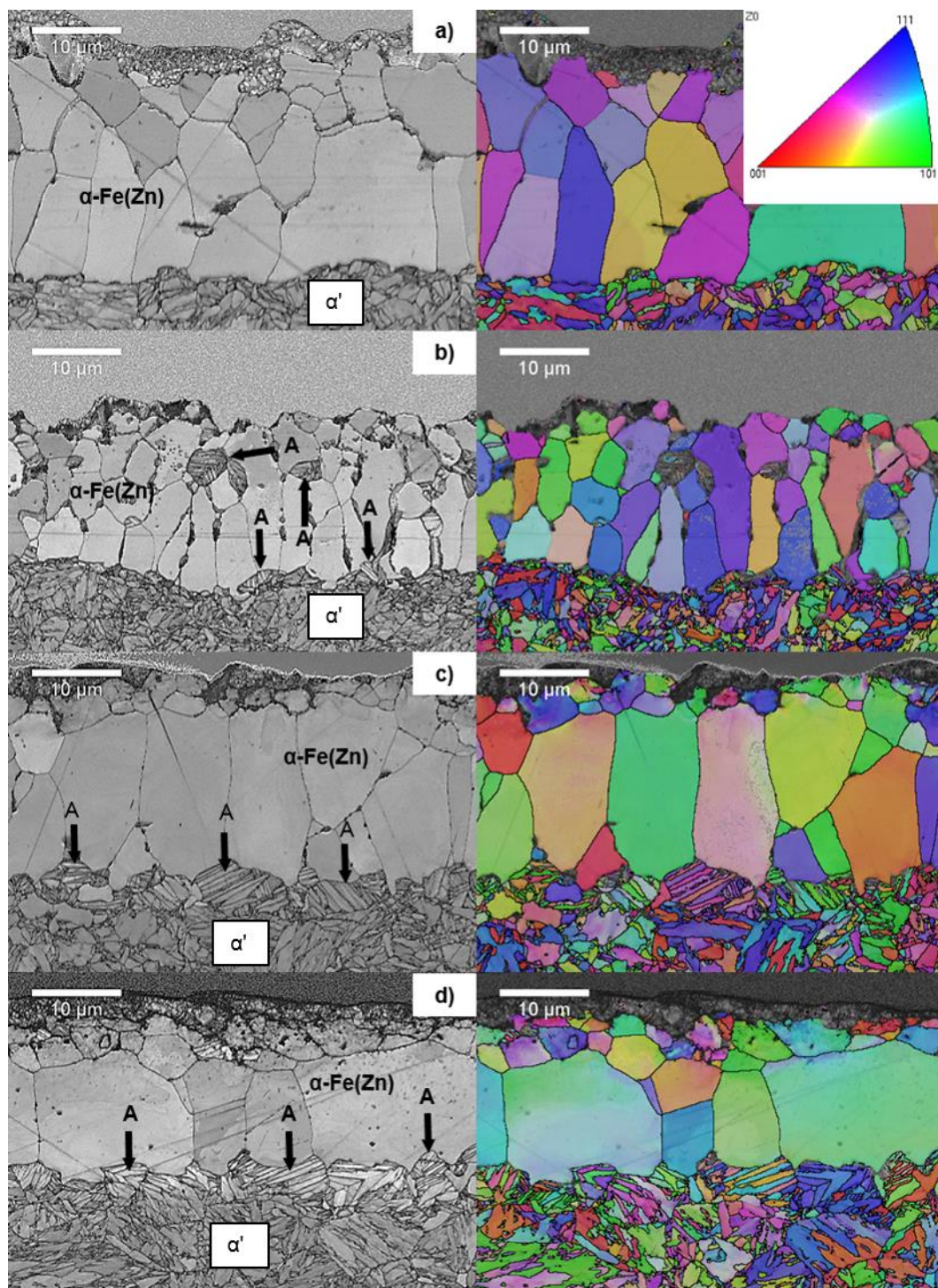




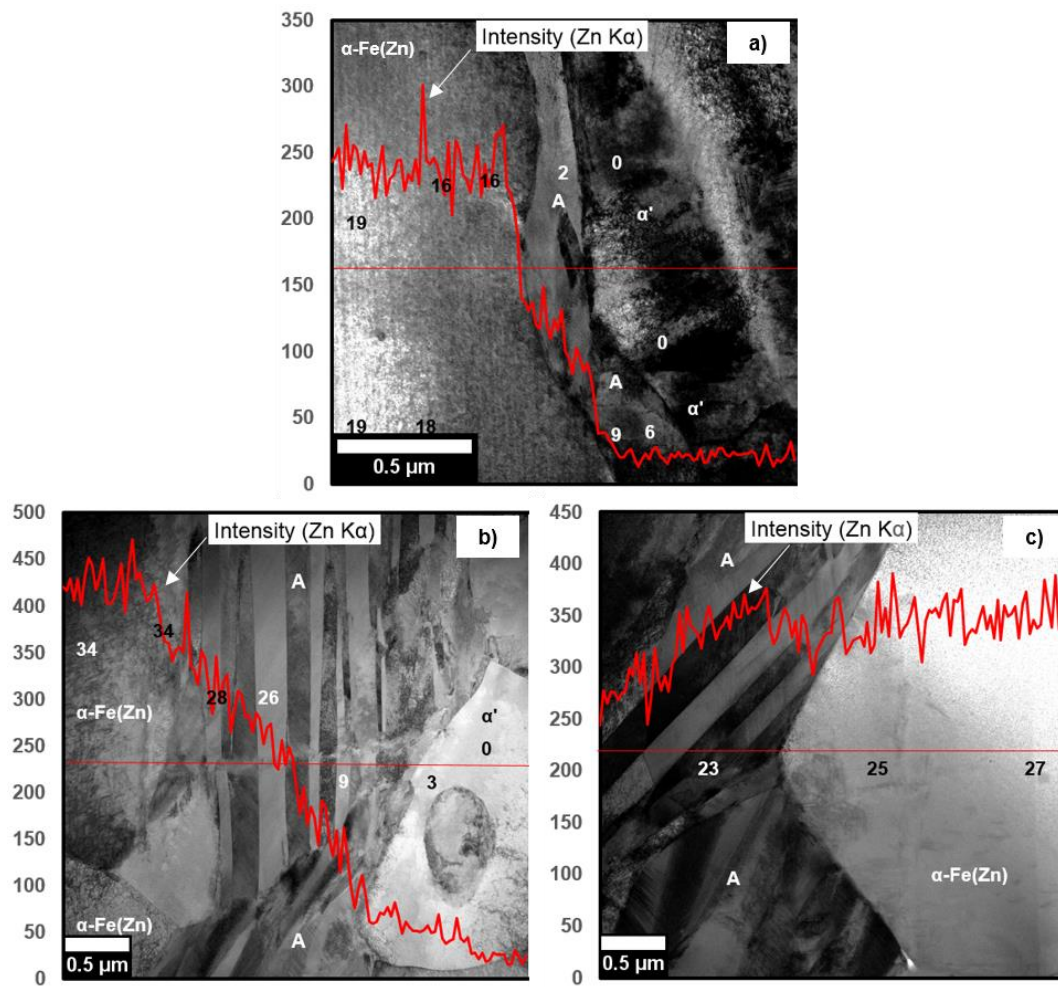
5



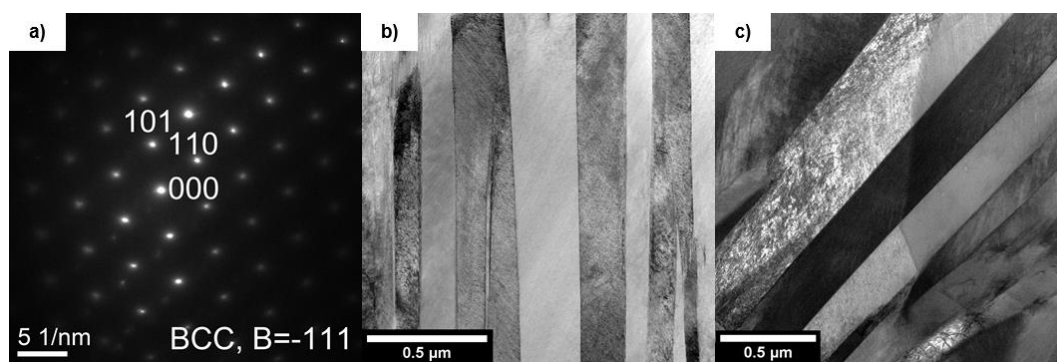




8



9



10